UNIVERSITY OF OKLAHOMA

GRADUATE COLLEGE

DESIGN, CHARACTERIZATION, AND ADDITIVE MANUFACTURING OF SHAPE MEMORY COMPOSITES

A THESIS

SUBMITTED TO THE GRADUATE FACULTY

in partial fulfillment of the requirements for

Degree of

MASTER OF SCIENCE

By

WESTON SLEEPER
Norman, Oklahoma
2020

DESIGN, CHARACTERIZATION, AND ADDITIVE MANUFACTURING OF

SHAPE MEMORY COMPOSITES

A THESIS APPROVED FOR THE

SCHOOL OF AEROSPACE AND MECHANICAL ENGINEERING

BY THE COMMITTEE CONSISTING OF

Dr. Yingtao Liu, Chair

Dr. Mrinal C. Saha, Co-Chair

Dr. M. Cengiz Altan

© Copyright by WESTON SLEEPER 2020

All Rights Reserved.

Acknowledgements

First, I would like to thank Dr. Yingtao Liu of the University of Oklahoma, whose role as an educator and research leader during my time at OU has been incredibly impactful. He has helped develop not only my skills as a practicing engineer, but also my curiosity and dedication to continuous education. Dr. Liu's enthusiasm regarding my participation in his research projects and his willingness to be adaptable to my concurrent professional obligations was essential for my success at the graduate level. His guidance throughout my undergraduate and graduate studies is something for which I will forever be grateful. It is that guidance that has encouraged me and given me the confidence to continually pursue new ideas that will make meaningful contributions to the scientific and professional communities. In addition to Dr. Liu's mentorship, I would like to thank Dr. Mrinal Saha, whose insights helped me to overcome hurdles in research that could have slowed progress. I certainly appreciate both Dr. Liu's and Dr. Saha's expansive knowledge regarding my research field and especially their willingness to take the time every week to review my progress and offer advice when necessary. In addition, I would like to thank the entire staff at the School of Aerospace and Mechanical Engineering for being available and helpful with a variety of matters and for being assets to our community working to advance the field of engineering. I'd also like to thank Billy Mays and Greg Williams of the Aerospace and Mechanical Engineering machine shop, whose practical knowledge and advice, along with their readiness to provide tools and materials, is instrumental in the success of the OU AME Department's extensive research network.

Additionally, I would like the thank my friends and colleagues in research, Blake Herren, Ben Hoelzel, Ryan Cowdrey, Noah Golly, and Colin Brey, whose enthusiasm and

character created a positive environment that facilitated progress. In addition to my research partners, I would like to thank my best friends Cody Cox, Ty Bruce, Jared Prewett, and Cameron Greer, who were all constant sources of positive encouragement and friendship.

Most importantly, I would like to thank my family. My parents, Janet and Scott Sleeper, instilled the importance of education in me at an early age and have always provided me with relentless encouragement. Also, I would like to thank my brother, Jared, and sister, Cady, who also have been supportive of my academic and professional pursuits. Finally, and with equal importance, I would like to thank my fiancé, DaLacy, who has been my inspiration throughout my time at OU and my cornerstone when overcoming adversity. All of these people have shaped me and helped me grow into the person I am, and I am eternally grateful for having them in my life.

Table of Contents

Acknowledgements iv

Table of Contents vi

Table of Figures viii

Table of Tables xi

Abstract xii

CHAPTER 1: INTRODUCTION 1

Section 1.1: Additive Manufacturing and Shape Memory Materials 1

Section 1.2: State of the Art of 3D Printing for Shape Memory Composites 2

Section 1.3: Direct Ink Writing (DIW) 8

Section 1.4: Thesis Outline 12

CHAPTER 2: OPTIMIZATION OF DIW PRINTING 13

Section 2.1: Optimization of Ink 13

Section 2.2: Mechanical Design and Optimization 15

Section 2.3: Software and Controls 17

CHAPTER 3: 3D PRINTED DIW SAMPLES 18

Section 3.1: Sample Modeling 18

Section 3.2 Material Preparation and Curing 21

Section 3.3 Multi-Layer Samples 24

Section 3.4: Proof of Concept 28

Section 3.5: Experimental Setups 31

CHAPTER 4: RESULTS AND ANALYSIS OF PRINTED SAMPLES 33

Section 4.1: Print Accuracy 33

Section 4.2: Tensile Tests – Carbon Black Non-Degassed..... 35

Section 4.3: Tensile Tests – Carbon Black Degassed..... 42

Section 4.4: Carbon Black - Resistance Tests 48

Section 4.5: Tensile Tests – MWCNT..... 53

Section 4.6: Thermal Cyclic Testing of MWCNT samples 56

CHAPTER 5: CONCLUSIONS AND FUTURE WORK..... 58

References..... 63

Table of Figures

Figure 1: Illustration describing FDM printing process [32] 3

Figure 2: Illustration describing DLP printing process [42] 6

Figure 3: Illustration describing DIW printing process [48] 8

Figure 4: Model of pneumatic DIW extrusion [9] 9

Figure 5: Model of piston driven DIW extrusion [9] 10

Figure 6: Model of lead screw DIW extrusion [9] 11

Figure 7: Cultures 3D DIW printer 16

Figure 8: CAD model of ASTM D638 Type V dogbone 18

Figure 9: CAD drawing of ASTM D638 Type V dogbone 19

Figure 10: Repetier-Host print preview of transverse infill 19

Figure 11: Repetier-Host print preview of longitudinal infill 20

Figure 12: Repetier-Host print preview of several layers 20

Figure 13: Repetier-Host print preview of aligned rectilinear infill pattern 21

Figure 14: Transverse infill of printed dogbone sample 24

Figure 15: Longitudinal infill of printed dogbone sample 25

Figure 16: Final layers of dogbone sample being printed 26

Figure 17: Copper tabs used as electrodes for conductivity testing 27

Figure 18: Second layer of conductivity dogbone being printed 27

Figure 19: CAD model of shape memory demonstration print 28

Figure 20: Folded MWCNT demonstration print 29

Figure 21: Unfolding process of MWCNT demonstration print 29

Figure 22: CAD model of second demonstration print 30

Figure 23: Carbon black demonstration print folded into box..... 30

Figure 24: Unfolding process of carbon black demonstration print 31

Figure 25: Average test section widths and thicknesses for carbon black samples..... 33

Figure 26: Average test section widths and thicknesses for MWCNT samples 34

Figure 27: Room temperature strain-to-failure trials for non-degassed 10 wt% carbon black, short fiber prints 36

Figure 28: Cross section of non-degassed 10 wt% carbon black, 1 wt% short fiber print 37

Figure 29: Cross section of non-degassed 10 wt% carbon black, 2 wt% short fiber print 37

Figure 30: Cross section of non-degassed 10 wt% carbon black, 3 wt% short fiber print 38

Figure 31: 2nd room temperature strain-to-failure trials for non-degassed 10 wt% carbon black, short fiber prints 39

Figure 32: Cross section of non-degassed 10 wt% carbon black, 1 wt% short fiber print 40

Figure 33: Cross section of non-degassed 10 wt% carbon black, 2 wt% short fiber print 40

Figure 34: Cross section of non-degassed 10 wt% carbon black, 3 wt% short fiber print 41

Figure 35: High temperature strain-to-failure trials for non-degassed 10 wt% carbon black, short fiber prints 42

Figure 36: Room temperature strain-to-failure trials for degassed 10 wt% carbon black, short fiber prints..... 43

Figure 37: Cross section of degassed 10 wt% carbon black, 1 wt% short fiber print 44

Figure 38: Cross section of degassed 10 wt% carbon black, 2 wt% short fiber print 44

Figure 39: Cross section of degassed 10 wt% carbon black, 3 wt% short fiber print 45

Figure 40: High temperature strain-to-failure trials for degassed 10 wt% carbon black, short fiber prints..... 45

Figure 41: Strain-to-failure trials of degassed and non-degassed 10 wt% carbon black, short fiber prints 46

Figure 42: High temperature cyclic loading of 10 wt% carbon black, short fiber prints . 47

Figure 43: Strain-resistance profile for 10 wt% carbon black, 1 wt% short fiber 49

Figure 44: Strain-resistance profile for 10 wt% carbon black, 2 wt% short fiber 50

Figure 45: Strain-resistance profile for 10 wt% carbon black, 3 wt% short fiber 51

Figure 46: Initial resistance (a) and resistance response by short fiber loading (b) 52

Figure 47: Resistance profiles of 10 wt% carbon black, 1-3 wt% short fiber prints 53

Figure 48: Strain-to-failure trials for 1.5 wt% MWCNTs, 0-7.5 wt% short fiber prints .. 54

Figure 49: 1.5% MWCNT, 0(a), 2.5(b), 5.0(c), and 7.5 wt%(d) short fiber prints 55

Figure 50: Thermal cyclic stress-strain curves of 1.5 wt% MWCNTs, short fiber prints 57

Figure 51: Thermal cyclic stress-time curves of 1.5 wt% MWCNTs, short fiber prints .. 57

Table of Tables

Table 1: 10 wt% Carbon black average test section dimensions by short fiber content... 34

Table 2: 1.5 wt% CNT average test section dimensions by short fiber content 35

Table 3: Results of 1st room temperature, degassed, carbon black, short fiber trials 36

Table 4: Results of 2nd room temperature, non-degassed, carbon black, short fiber trials 39

Table 5: Results of room temperature, degassed, carbon black and short fiber trials 43

Table 6: Maximum stress for each loading cycle of high temperature strain trials..... 47

Table 7: Stress reduction per cycle of high temperature strain cycles..... 48

Table 8: Resistances by short fiber content of strained 10 wt% carbon black prints 52

Table 9: Results of room temperature, 1.5 wt% MWCNT strain-to-failure trials..... 54

Table 10: Tensile stress throughout thermal cyclic trials 58

Abstract

Direct Ink Writing (DIW) is an additive manufacturing method that utilizes a reservoir of fluid that is precisely extruded to construct 3-Dimensional (3D) structures from layering 2-Dimensional (2D) patterns. Fluids used in DIW printing can vary from in-situ, UV-cured resins to thermosetting epoxies that are solidified following the printing process. This thesis explores the latter fluid, specifically those epoxies which possess shape memory abilities. The shape memory function allows a solid, printed component to deform elastically when its temperature exceeds the glass transition temperature (T_g). However, shape memory epoxies traditionally lack the necessary fluid qualities for printing. By forming a composite ink and integrating a network of multiwalled carbon nanotubes (MWCNTs) or carbon black within the uncured fluid profile, the resulting multiphase ink can possess the requisite fluid rheology to facilitate 3D printing through the DIW process. This thesis examines the development and characteristics of two novel DIW inks, one supported by carbon black and the other supported by MWCNTs. In both cases, the composite ink, made printable by either its carbon black or MWCNT content, is further reinforced with VMX24 carbon short fibers. The varying short fiber content revealed various trends in conductivity and mechanical characteristics of the finished 3D printed samples. For the carbon-black based ink, the resulting prints proved themselves to be potential candidates for strain sensors, given their strong electromechanical response at low strain. For both MWCNT- and carbon black-based epoxy inks, the shape memory effect of the base epoxy was retained, resulting in novel DIW inks that are both functional and mechanically resilient.

CHAPTER 1: INTRODUCTION

Section 1.1: Additive Manufacturing and Shape Memory Materials

Additive manufacturing, or the process of generating an item through means of material deposition rather than material subtraction, offers a variety of new possibilities in terms of rapidly producing complex geometries [1]. 3D printing, a more general term to describe additive manufacturing processes, has continuously expanded since its inception to include a wide array of material options and material deposition methods [2]. With such expansion has come the ability to print fiber reinforced composites, nanocomposites, metals, ceramics, and conventional thermoplastics [3-8]. The most common 3D printing processes include fused deposition modeling (FDM), direct ink writing (DIW), selective laser sintering (SLS), and stereolithography (SLA), aggregating a total of 96% of the total 3D printing market [9-12].

As 3D printing continues to grow in popularity, the various processes are generating more mechanically sound and functional materials, which include smart materials such as shape memory epoxies and polymers. Shape memory materials are those that possess the capability to recover their original structure following loading from an external stimulus that resulted in deformation [13-15]. This transition is typically controlled by thermal cycling in which the transition temperature is exceeded, allowing the material to revert to its original structure from the temporary, deformed structure. Sometimes referred to as "smart" or "intelligent" systems, shape memory materials are usually the resulting composition of multiple components. These materials behave according to the specific tuning of the constituent components, which in turn regulates their shape memory response.

The integration of multiple components generates highly functional composites and alloys that expand the mechanical properties and practical usefulness of the shape memory materials beyond the constituent shape memory materials [16]. Shape memory materials have long been studied because of their potential applications for deploying equipment or systems in traditionally impractical areas of work. Some of these regions include the human body, which in turn has opened a new field of research for shape memory composites in the community of biomedical engineering [17-21]. In addition, these materials have broad potential applications in the fields of energy production, space exploration, textiles, civil engineering, bionics engineering, energy, electronic engineering, and even household products [22-27].

Section 1.2: State of the Art of 3D Printing for Shape Memory Composites

As 3D printing expands, so does the research field for the supporting materials and methodologies. With widened research horizons, the possibilities for printing advanced, or "smart" materials are increasing, enhancing prospects to print advanced materials in the various 3D printing processes mentioned in Section 1.1. Among the most common methods currently compatible with and suitable for printing composites and shape memory materials are FDM, digital light processing (DLP), and DIW [28].

FDM, one of the most common 3D printing processes, involves a solid material being extruded through a heated nozzle, liquifying or softening the material to the extent necessary for extrusion and subsequent deposition [29]. In this process, materials must be manufactured into a wire geometry, referred to as a "filament", which must be spooled to be compatible with most FDM processes. That filament is unspooled and fed continuously via extruder motors which act as rollers, generating the force for extrusion. A diagram

illustrating the FDM printing process is shown below in Figure 1. This technique is best suited for chemically consistent and stable materials like ABS (Acrylonitrile Butadiene Styrene) and PLA (Polylactic Acid), which are among the most common materials for FDM filaments [30]. Yang, et al., however, has shown that the manufacturing of shape memory filaments through practical and novel methodologies is possible. In their study, they extruded shape memory polymer (SMP) pellets through a series of motors and dies to fabricate and wind the filament, which could be then integrated into existing FDM printer hardware in the place of commercially available PLA or ABS filament [31].

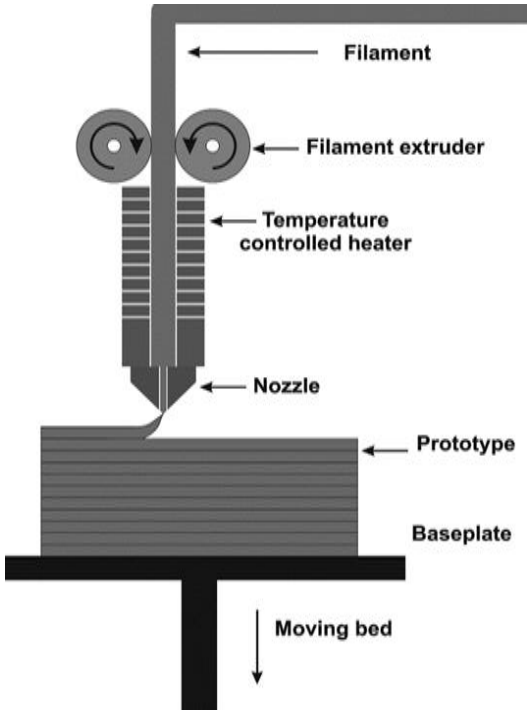

Figure 1: Illustration describing FDM printing process [32]

Liu et al. further illustrated the capabilities of the FDM process by integrating particles of silicon carbide and graphite into an otherwise ordinary PLA filament. In generating this composite filament, they were able to enhance thermal and electrical conductivity properties. In addition to enhanced conductivity properties, the integration of

the silicon and graphite particles helped to improve the shape memory function of the PLA-based printed components [33]. Not only did the silicon and graphite particles decrease the time for shape recovery, they improved the recovery percentage of the printed component. Liu et al. demonstrated homogeneous suspension of silicon carbide and graphite as the means of producing FDM composite materials. In some studies, FDM composites have also been printed with continuous carbon fiber, drastically improving the mechanical properties of the printed samples [34].

In addition to showing the effectiveness and printability of composite PLA filaments for the FDM process, high weight loadings of composite filament materials have also been shown. Liu et al. again demonstrated the capabilities of FDM by successfully printing silicon carbide and carbon filled PLA with loadings as high as 60 wt%, a range typically reserved for non-extrusion-based 3D printing methods. High loadings also proved effective for improving the shape memory response, as response rate and total response time was correlated to the thermal conductivity of the highly loaded composite print samples [35]. While loading to this extent is not necessarily possible for all materials and 3D printing methods, it illustrated the inherent benefits to the shape memory effect of high loading of the compositing materials. These benefits are especially noticed when those materials possess high thermal conductivity and the shape memory effect of the base material is thermoresponsive.

It has also been shown that the suspension of fibers in elastomer scaffolds with FDM, followed by a subsequent silicone encapsulation process, is effective in generating a programmable, dynamic shape memory material [36]. Programmability regarding shape memory response, mechanical properties, and conductivity properties allows for the

ultimate flexibility concerning implementation possibilities for a given material. Furthering the discussion on tunability and material programming, hot and cold programming methods have proven effective for certain FDM-compatible materials. In addition to having tunable attributes, it is critical for materials, especially in the FDM process, to be receptive to quality-improving post processing. Opportunities for further processing FDM composites after the printing process have only been explored to limited extents. However, post—print annealing has proven effective in improving the compressive and tensile performance of shape memory polymers compounded with traditional PLA filaments [37].

Further expanding the versatility of the FDM platform for printing functional shape memory materials, efforts have been made to expand the shape memory capabilities of FDM composite filaments through the introduction of the triple shape memory effect. While traditional shape memory materials have dual shape memory, activated by a single transition temperature, a triple shape memory effect allows shape memory activation across a range of temperatures [38]. The triple shape memory effect allows shape memory materials to memorize two temporary shapes and meet more diverse requirements. Triple shape memory is achieved through either the use of a dual shape memory polymer (SMP) network, with each network having a unique transition temperature, or through the use of a single SMP featuring a wide transition temperature range [39].

The DLP process has also been utilized to print functional shape memory components. The DLP process, unlike FDM, utilizes photocuring liquid resins to generate printed components. A liquid bath with a transparent base has the cross section of the desired print projected from below, curing a thin layer of the photocuring resin to a vertically travelling build plate [40]. As the build plate moves up, a new layer of the print

is projected, curing successive 2D images of the print to generate the 3D component [41]. An image detailing the DLP printing process is shown below in Figure 2.

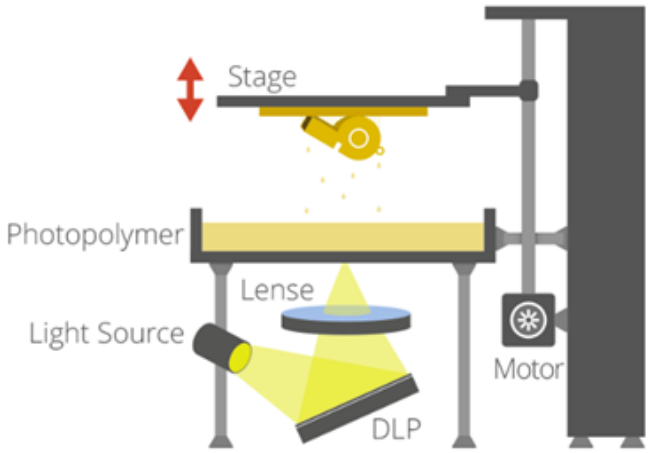

Figure 2: Illustration describing DLP printing process [42]

Li et al. showed the capabilities of the DLP platform in generating functional shape memory components by utilizing a photo-sensitive base material featuring high recovery stress to produce a variety of microlattice structures. Bisphenol-A glycerolate dimethacrylate (BPAGMA), on its own, provides the functional characteristics of shape memory and ideal mechanical properties, but is not suitable for the DLP platform due to the unusually long UV exposure required for curing. When combining BPAGMA with 1,4 Butanediol Dimethacrylate (BDDMA), a more UV responsive molecule, the resulting resin was highly successful in satisfying the high-resolution standards common to the DLP printing platform [43]. The slight tailoring of the BPAGMA base by incorporating BDDMA generated a unique resin whose final, fully UV-crosslinked form was highly stable and able to maintain, to a high degree, the positive characteristics of the BPAGMA foundation.

Beyond simply printing shape memory materials with DLP methods, other work has been produced to increase the shape memory performance of novel photosensitive resins that are compatible with the DLP process. While the field of DLP-adaptable resins is narrow, resins featuring the 1, 6-hexanediol diacrylate (HDDA) crosslinker, especially at high loadings, exhibit excellent shape recovery characteristics [44]. The high-performing qualities of such resins make them potential foundations for fiber-reinforced, DLP-printed composites, although this area has been explored to a limited degree.

One of the studies existing to explore carbon-based reinforced composites integrated MWCNTs to reveal possibilities for the DLP platform to provide functional strain sensors. This study ultimately concluded that the added sensing functionality presented by incorporating MWCNTs not only resulted in electrically conductive printed components, but also slightly improved mechanical function [45].

Additionally, work has been done in the field of printing shape memory materials with DLP processes for applications regarding flexible electronics. By employing oligomer melts, an effective method for utilizing the DLP processes to 3D print conductive shape memory components was established without the use of carbon compositing structures [46]. While retaining the high-resolution standards of the DLP process, these conductive prints were capable of performing with high precision in a variety of potential sensor applications while retaining the oligomer's shape memory properties.

The direct ink writing process, unlike DLP and FDM, is a niche method involving a fluid being extruded through a nozzle to lay successive cross-sectional areas in order to construct the 3D structure. Mechanically, there are a few variations in terms of how that fluid is extruded from the reservoir, each with their own perceived benefits. However,

regardless of the specific details of each individual process, which will be discussed in a later section, an external force is generated on a fluid reservoir to generate the extrusion force [47]. A schematic of the fundamental principle of DIW is shown below in Figure 3. Because the epoxy base material selected for this study is most easily manipulated in its uncured form, and due to the integration of carbon substructures to generate composites, the DIW process was the most practical option for this study. Additionally, relative to DLP and FDM, the existing research field pertaining to DIW printing fiber reinforced composites is limited.

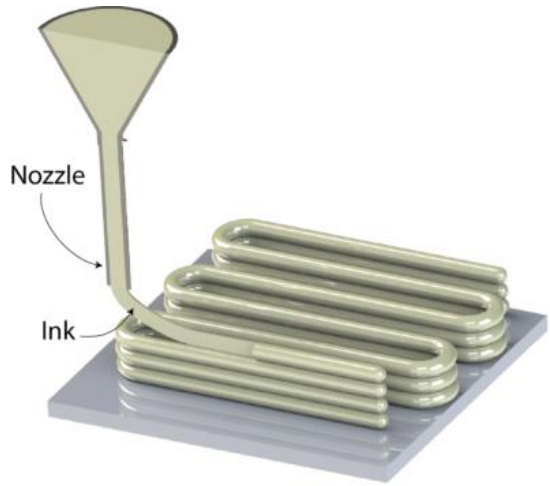

Figure 3: Illustration describing DIW printing process [48]

Section 1.3: Direct Ink Writing

The first DIW method, air pressure extrusion, as shown below in Figure 4, utilizes a free-floating plunger driven by an air pressure source. The continuous application of pressure on the rear of the plunger translates through the plunger into the fluid reservoir, causing consistent extrusion through the nozzle. The main controls to manage extrusion

rate is simple the regulation of the supplied air pressure. This method is limited by the available volume for the fluid reservoir but offers precise tuning options for extrusion rate.

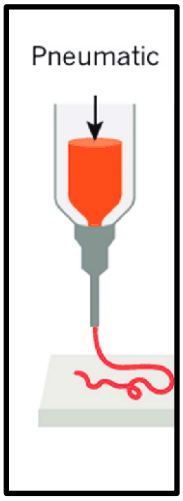

Figure 4: Model of pneumatic DIW extrusion [9]

The second DIW method is linear, mechanical piston displacement, shown below in Figure 5. In this process, a lead screw is rotated with a servo motor. The lead screw is mechanically bound to a travelling block that translates the rotation of the screw into a linear force, plunging the piston to extrude the print material from the fluid reservoir. This method is also limited in volume, but has practical benefits because standard, disposable syringes are used as the fluid reservoir.

Figure 5: Model of piston driven DIW extrusion [9]

The third method is lead screw extrusion, shown below in Figure 6. Similar to the linear, mechanical displacement process, this process utilizes a servo whose lead screw has tight tolerances with the side walls of the fluid reservoir. As the lead screw rotates, the axial force interaction between the lead screw and the fluid causes extrusion out of the nozzle. The lead screw is continuously fed fluid by a secondary, pressurized reservoir of print material [9]. This method has the benefit of large reservoir volumes, but there is the inherent issue of material buildup on the hardware because the reservoirs are non-disposable.

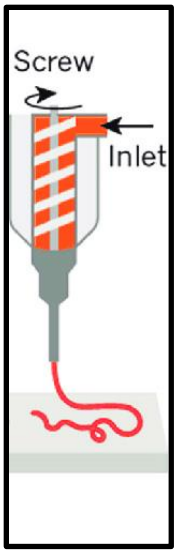

Figure 6: Model of lead screw DIW extrusion [9]

Because of the commercial availability and modularity of linear displacement DIW systems, and the inherent benefits that are provided by the ease of tuning those systems, it was the piston-type process that was used as the foundation for this study. While each system does have advantages, the challenges of printing functional shape memory composite epoxies with the DIW process are shared amongst the three methods. These limitations will be discussed in greater detail in Chapter 2.

DIW has been shown, on numerous occasions, to be an effective method of 3D printing shape memory materials. Chen, et al. showed that DIW methods, coupled with a two-stage curing process, was effective in 3D printing shape memory epoxy utilizing UV assist. The epoxy oligomer, providing the foundation of the shape memory functionality, was coupled with a UV cured resin. The UV resin, offering little in the sense of mechanical durability, provided the functional pathway to make in-situ curing possible. In-situ curing is a necessity in order to 3D print since most shape memory epoxies do not possess the fluid properties required to stack multiple layers of ink [49].

Apart from the printing of epoxies, other studies have shown DIW to be a useful method of printing silicones with shape memory properties. Wu, et al. illustrated a novel approach of printing functional silicone laden with gas-filled polymer spheres, tailoring the mechanical characteristics of the silicone component by altering the concentration of spheres and by selecting different polymers based on their glass transition temperature [50].

Section 1.4: Thesis Outline

The objective of this thesis is to characterize two general types of novel DIW epoxy inks, the first utilizing carbon black as the supporting material and the second using MWCNTs, with each featuring carbon short fibers in various concentrations to provide reinforcement. Beyond mechanical characterization, the objective is also to explore possible applications for the carbon black-based epoxies to be used as sensing elements due to their consistently conductive behavior. Chapter 2 will outline the properties and composition of both types of epoxy inks and the mechanical design and software of the printer used to print those epoxies with DIW methods. Chapter 3 will detail the printing process, from sample inception in computer aided design (CAD) models to sample printing with the equipment described in Chapter 2. Chapter 3 will also cover the retention of the shape memory effect for both carbon black- and MWCNT-based epoxies, as well as detail the testing process by which the printed samples were characterized. Chapter 4 will detail the quantitative and qualitative results regarding those characterization tests. Finally, Chapter 5 will summarize the findings and provide a synopsis of the preceding information, while detailing future opportunities related to this work.

CHAPTER 2: OPTIMIZATION OF DIW PRINTING

The optimization process to make possible the printing of functional shape memory composites with the DIW method focused on two subjects primarily. The first subject was the tailoring of the fluid characteristics of the uncured composite ink in order to provide the requisite yield strength and fluid rheology to support extrusion and the stacking of layers. The second focus was aligning the software and controls to facilitate the successful and consistent extrusion of that composite ink.

Section 2.1: Optimization of Inks

By prioritizing the printability of the uncured ink, the content of the ink itself was varied in a trial-and-error process to allow a range of short fiber loading for each fluid type. The variance of the composite components, along with a novel approach of combining two curing agents, Epikure W and Epikure 9553, each with specific rheological effects on the ink, made printing with relatively high resolution possible. The objective was to find the maximum possible loading of the reinforcing carbon substructures that still allowed printing through a 20-gauge Leur-Lock syringe nozzle.

Studies focused on CNT inks for DIW purposes have utilized a range of weight loadings, from 1 wt% to 8 wt%, with higher loadings typically being better received by ink jetting processes [51].

First, for the MWCNT-based composite inks, it was found that in order to generate the requisite yield strength for printing without support from VMX24 short fiber, 1.5 wt% MWCNT was ideal. Loading nanotubes at 1.5 wt% allowed for reliable printing with a 20-gauge nozzle between zero and 7.5 wt% VMX24 short fiber without clogging the nozzle.

Traditional loading of carbon short fiber for DIW applications does not exceed 2.0 wt% [52]. However, for the carbon black-based composite inks, to achieve the same requisite yield strength to facilitate printing, 10 wt% was required of carbon black. This base loading of carbon black allowed for up to 3.0 wt% loading of the VMX24 carbon short fiber before nozzle clogging became consistently problematic.

Regarding the use of both Epikure 9553 and Epikure W curing agents, because of their unique effects on Epon 862's curing process, both presented benefits to the printing process. Referencing the previously mentioned work by Chen, et al., in-situ curing was found to be beneficial to stacking for both MWCNT- and carbon black-based inks. The Epikure 9553 component, because of its curing capabilities in ambient temperatures, allowed for a slowly activating in-situ curing following the mixing process. The added rigidity provided by the partially cured preceding layers supported the following layers, maintaining the dimensional accuracy of the print when compared to the print model. However, the same ambient curing feature of Epikure 9553 that makes it useful also shortens the pot life of the ink. If Epikure 9553 is used as the sole curing agent at the concentration recommended by the manufacturer, Epikure 9553 and Epon 862's pot life is approximately 30 minutes. It should be noted that pot life, while measured by a standardized method from the manufacturer, is subject to the application. For this application, with the addition of carbon components, the functional time of an Epon 862 and Epikure 9553 epoxy fluid is between 5 and 10 minutes due to nozzle clogging issues. However, with the use of Epikure W as the sole curing agent with Epon 862, the pot life of the resulting epoxy, as described by the manufacturer, exceeds 10 hours. With only Epikure W, however, no in-situ curing is provided and a high heat curing process is

required, which caused part deformation. Therefore, the utilization of both curing agents was necessary to provide adequate pot life and support in-situ curing.

Section 2.2: Mechanical Design and Optimization

In terms of hardware, the 3D printer used for all sample preparation was a commercially available Tissue Scribe bioprinter from 3D Cultures. This printer, shown below in Figure 7, features the linear displacement extrusion system mentioned previously in Section 1.2 and operates on a cartesian navigation system. With this printer, a 3 mL syringe and plunger are secured in a machined aluminum housing, which is actuated by an extruder motor-driven lead screw. As the extruder motor turns, the plunger drives fluid from the reservoir out of the Leur lock nozzle and onto the build plate. Because of the curing process of Epon 862 with the dual Epikure 9553 and Epikure W curing agents, the build plates were covered in Teflon tape, which made removal post curing possible.

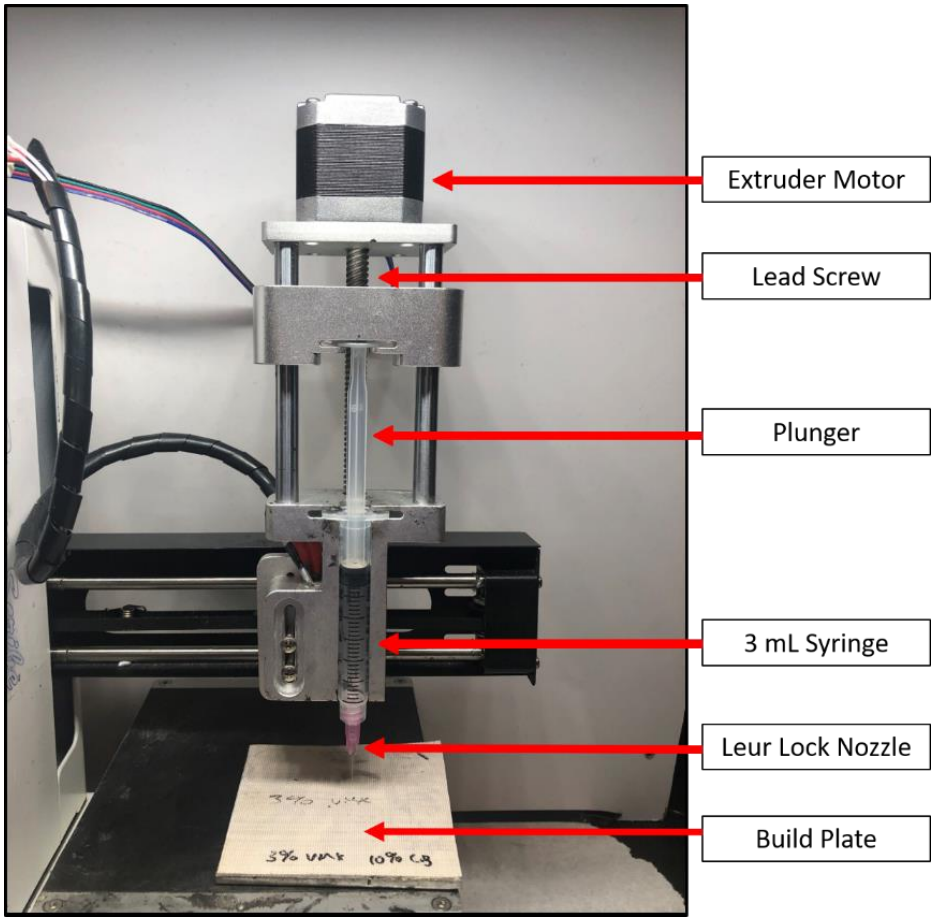

Figure 7: Cultures 3D DIW printer

Beginning with extrusion rate and travel speed, it was found after a trial-and-error process that a travel speed of 2 $\frac{mm}{s}$ and extrusion rate of 25 $\frac{steps}{mm}$ were optimal for ensuring continuous extrusion. Infill patterns and density varied only for different types of samples being generated. For mechanical testing, 100-percent infill density was utilized in conjunction with a rectilinear infill pattern. For conductivity tests, specifically those relating resistance to strain, a 90-percent infill density with an aligned rectilinear pattern was utilized. These patterns will be covered in more detail later in Section 3.1.

Section 2.3: Software and Controls

The slicing software, Repetier-Host, was used to generate g-code and also to tune the printing parameters mentioned previously in Section 2.2. Among the parameters that were tailored using Repetier-Host were the number of layers printed, infill density and pattern, and travel speed for perimeters and infill sequences. Repetier-Host, in addition to offering explicit controls for certain parameters, also offers a g-code editor, which allows custom g-code to be placed anywhere in the printing process. This software was used to input a homing sequence at the beginning of each print, ensuring that the print was placed on the Teflon covered build plate.

CHAPTER 3: 3D PRINTED DIW SAMPLES

Section 3.1: Sample Modeling

All printed samples were based off the ASTM D638 Type V dogbone [53]. The 3D model used to generate the g-code for the printed dogbone samples studied throughout this paper is shown below in Figure 8. For this dogbone standard, the sample has an ideal thickness of 3.20 mm throughout and a test section width of 3.18 mm.

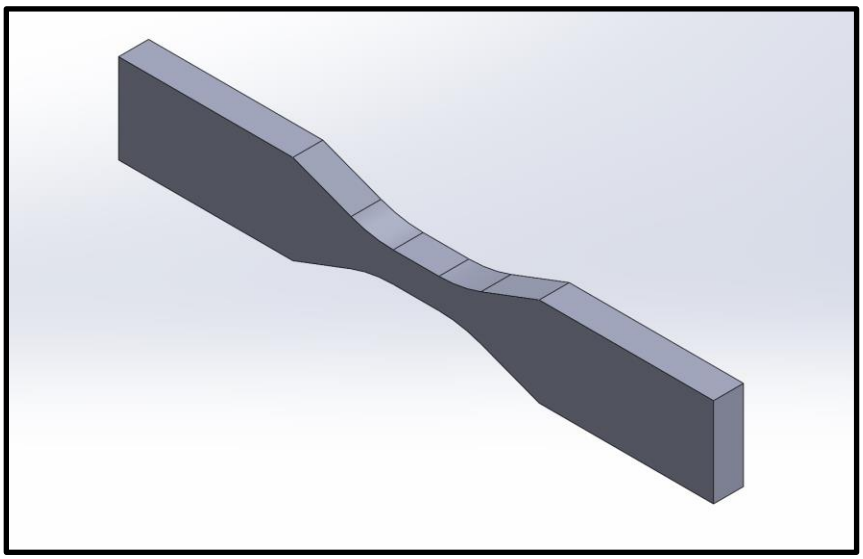

Figure 8: CAD model of ASTM D638 Type V dogbone

Below, Figure 9 is the dimensional drawing of the D638 Type V dogbone. All dimensions shown are in millimeters.

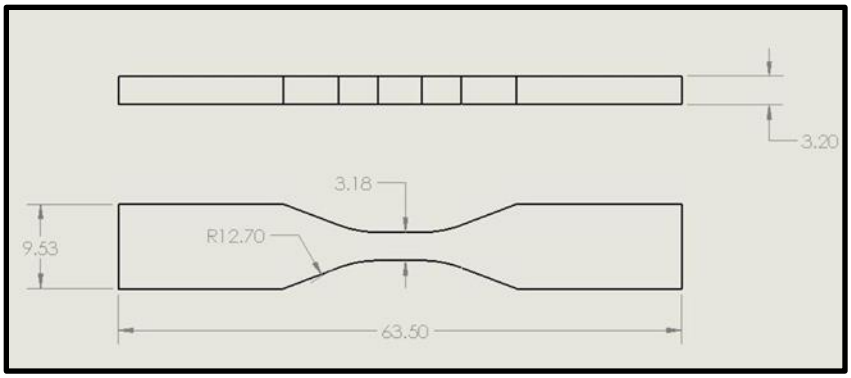

Figure 9: CAD drawing of ASTM D638 Type V dogbone

An example of the 100% infill, rectilinear process is shown below. With the rectilinear pattern, each successive layer is laid perpendicular to the previous layer. Figure 10 shows the first infill layer, which is laid in the transverse direction. Prior to printing the first perimeter path and beginning infill on the first layer, the slicing software, Repetier-Host, provides a function to print a skirt path around the sample. This is visible in Figure 10 below and was utilized to remove the slight aeration that typically occurs at initial extrusion through a new syringe nozzle, helping to maintain continuity during the printing of the actual dogbone sample.

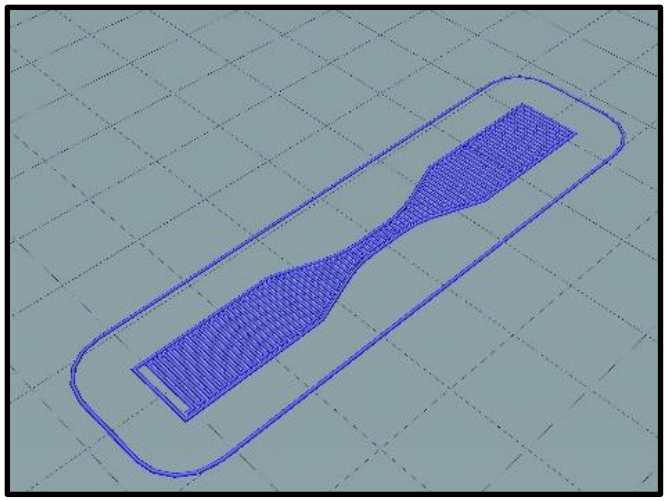

Figure 10: Repetier-Host print preview of transverse infill

Figure 11 shows the second layer, which is in the longitudinal direction. Prior to this infill layer, a perimeter path is laid, which functioned as a physical barrier containing the slight overextrusion as the nozzle sweeps near the edges of the sample.

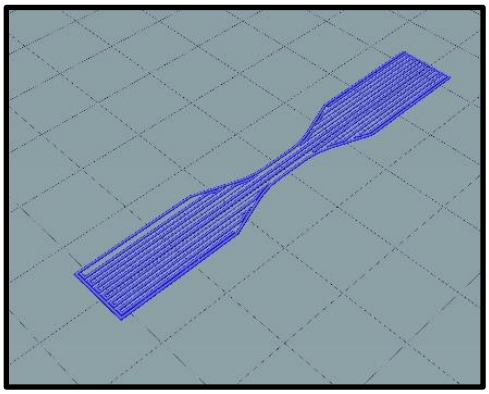

Figure 11: Repetier-Host print preview of longitudinal infill

Figure 12 shows the combination of the layers for a total of six repetitions, generating a full ASTM D638 dogbone sample.

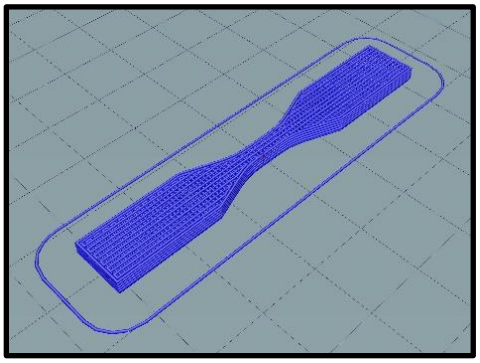

Figure 12: Repetier-Host print preview of several layers

For non-mechanical samples, which were printed to monitor electromechanical response in the electrically conductive composite samples, the same ASTM D638 samples were printed but using an aligned rectilinear pattern in which all layers were printed in the longitudinal direction. An example of the aligned rectilinear infill pattern is shown below

in Figure 13. It is important to note that while these models of the print path clearly illustrate discontinuities between the bordering print paths, continuity is maintained due to intentional overextrusion. Overextrusion, when controlled precisely via tuned ink characteristics and proper nozzle selection, is a requirement to maintain continuity and prevent macroscopic porosity, which would ultimately lead to stress concentrations and obvious structural defects. Overextrusion and the practical implementation of these print paths will be explored later in Section 3.3.

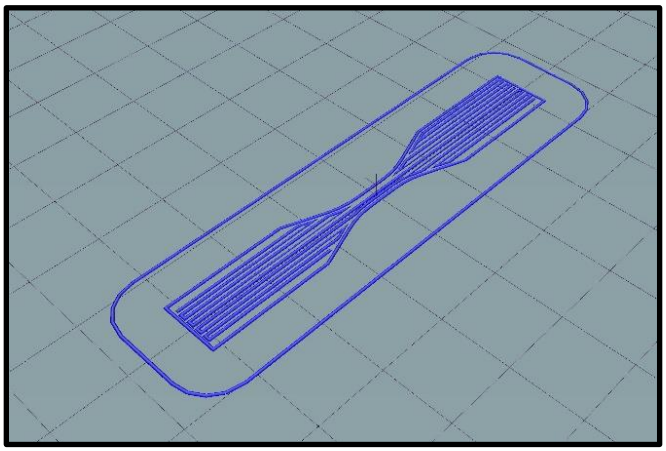

Figure 13: Repetier-Host print preview of aligned rectilinear infill pattern

Section 3.2 Material Preparation and Curing

In terms of material preparation, multiple avenues of shear mixing, manual mixing, and degassing were explored to increase the printability of the epoxy ink and optimize the mechanical properties following printing. The effects, both qualitative and quantitative, of the different physical mixing processes will be discussed in Chapter 4. The three components to the shape memory epoxy base fluid were the resin, Epon 862, and the two curing agents, Epikure 9553 and Epikure W. The three components are all manufactured by and procured from Hexion.

Epon 862, (Diglycidyle Ether of Bisphenol-F) is the resin base for all epoxy inks used in this analysis. Epikure 9553, a polyamine, has a relatively low room temperature viscosity, described by its manufacturer as being less than 10 cP [4]. The Epon 862 resin, when combined with Epikure 9553, will cure at room temperatures according to manufacturer specifications, as discussed in Chapter 2.1. Epikure W, a non–meta-phenylenediamine aromatic amine, while being still considered low viscosity, has a room temperature viscosity between 100 and 350 cP. Epon 862, when combined with Epikure W, requires elevated temperatures for curing to be completed, although there are multiple possible temperature ramping procedures. The ramping procedure and time spent at each temperature affects not only the curing time but the properties of the resulting epoxy [4]. Each curing agent, because of their significantly different fluid profiles, contribute to the printability of the composite ink. Because of Epikure 9553's tendency to cure at room temperature, it shortens the pot life of the epoxy ink, while Epikure W's high temperature requirement for curing extends the pot life indefinitely when used on its own. The combination of the two agents produces an ink with a pot life of approximately 40 minutes after being thoroughly dispersed. This provides a pot life suitable for 3D printing while still inducing in-situ curing in ambient temperatures without an external stimulus.

The manufacturer's recommended resin to curing agent weight ratios for Epikure 9553 and Epikure W, when combined with Epon 862, are 100:17 and 100:26 respectively [4]. Due to the novel approach utilizing both agents, and their respective effects on the ink rheology, the optimal concentrations for Epikure 9553 and Epikure W were found to be 100:8.5 and 100:13 respectively, or exactly half of the recommended ratios.

Prior to the addition of the curing agents to the resin, however, the carbon-based reinforcement was added to the Epon 862. First, for both the carbon black- and MWCNT-based inks, the VMX24 carbon short fiber, procured from Solvay, was added and hand mixed into the resin for approximately 5 minutes. VMX24 short fibers have a density of 1.9 $\frac{g}{cm^3}$, a diameter of 10 μm, and residual length of 150 μm [54]. After initial mixing, the MWCNT or carbon black components were added at their desired concentration and again hand mixed for 5 minutes. The MWCNTs, having a density of 2.1$\frac{g}{cm^3}$, an average diameter of 50-90 nm, and an aspect ratio greater than 100, were manufactured by and procured from Sigma Aldrich [55]. Also, the carbon black was manufactured by and procured from Sigma Aldrich, having an average particle size of less than 500 nm and a density of 0.056 $\frac{g}{cm^3}$ [56]. Once an initial dispersion of both components was achieved manually, a stir bar was then added to the composite ink and the fluid was shear mixed at 400 rpm for 45 minutes.

Following the shear mixing to ensure dispersion of the carbon components, the two curing agents were added dropwise until the aforementioned concentrations were achieved. After adding the curing agents, the mixture was again shear mixed with a stir bar for 5 minutes at 400 rpm. For some samples, the ink was then degassed at room temperature for 5 minutes to remove aerated pockets induced by both manual and shear mixing, which will be further explored in the following chapters.

Following the printing process, because of the unique behavior and chemical content of the ink, a two-stage curing process is utilized to activate both curing agents. The first stage begins at the commencement of the printing phase, in which the ambient curing

capabilities of Epikure 9553 solidify the printed sample. After a 12-hour period of curing at room temperature, the sample is then placed into an oven at 180 °C for two hours, activating the Epikure W component.

Section 3.3 Multi-Layer Samples

During the printing process, as stated previously in Section 3.1, an alternating printing pattern was utilized to generate the ASTM D638 dogbones. Below, in Figure 14, the base layer, printed in the transverse direction, can be seen. Comparing these images to the model images above in Section 3.1, it is clear the print path illustrated does not identically reflect the true print infill. Due to consistent, controlled overextrusion, the line width of the print path is slightly wider than the inside diameter of the nozzle. Because of overextrusion, compensations are made in the g-code to allow adequate center-to-center distance between successively placed lines in the print path. As illustrated in the images, there is total continuity, thus reducing the likelihood of introducing porosity, as the slight interference between each line ensures that it combines with the previously laid line.

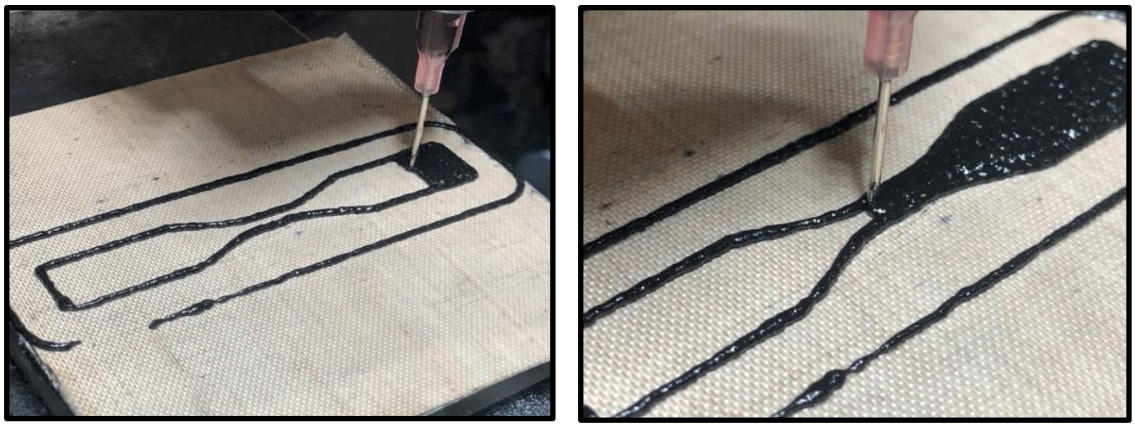

Figure 14: Transverse infill of printed dogbone sample

As modeled above in Section 3.1, the second layer is then laid in the longitudinal direction. Again, as in the transverse layers, overextrusion creates interference between adjacent print lines to generate a continuous layer. An example of the longitudinally oriented second layer can be seen below in Figure 15.

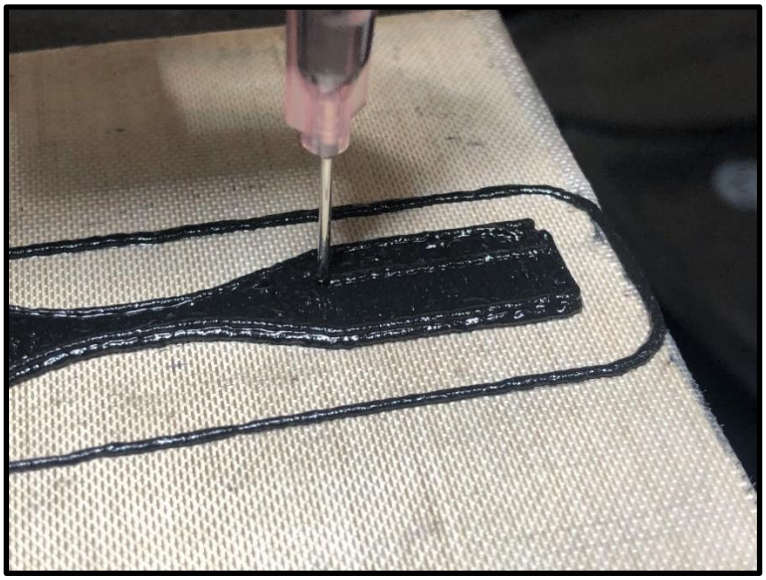

Figure 15: Longitudinal infill of printed dogbone sample

Finally, to illustrate the third layer, Figure 16 below shows the repeating of the transverse infill pattern laid on the first layer. This image, along with Figure 15 above, illustrates the unique capabilities of the liquid ink, which, due to the specifically tailored fluid profile and yield strength, can be stacked repeatedly.

Figure 16: Final layers of dogbone sample being printed

The printed structures shown above were all used to verify the mechanical characteristics of the cured composite ink. However, mechanical performance is only one focus of this study. Because of the previously discussed electrical conductivity of both composite materials examined, special two-layer dogbone samples were generated to study electromechanical response when strained in a manner similar to the mechanical tests. Those samples had copper tape carefully placed between the first and second layer of the print. The copper tape protruding from the printed sample served as an electrode to monitor electromechanical response as the dogbone is strained. Again, as mentioned in Section 3.1, these samples were printed at 90% infill to allow for the use of the aligned rectilinear infill pattern. Because of intentional overextrusion, however, total continuity was maintained with 90% infill density. Below, Figure 17 illustrates the first layer of the electromechanical samples being printed with an alternating transverse and longitudinal infill patterns. It should be noted all data collection and electromechanical characterization was done with samples printed only in the longitudinal direction. This particular sample being printed featured a transverse first layer and longitudinal second layer. The copper tape can be seen protruding from the first grip tab printed on this sample.

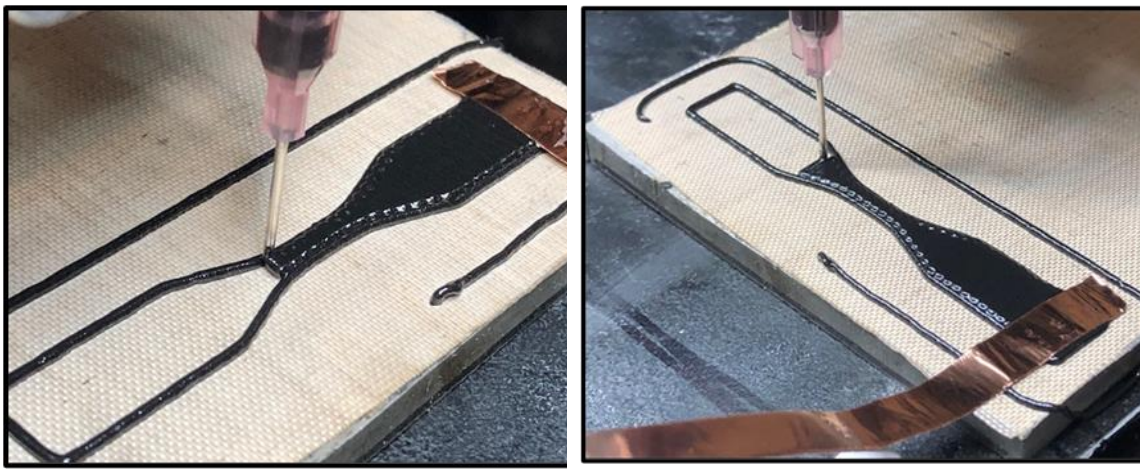

Figure 17: Copper tabs used as electrodes for conductivity testing

Figure 17 above shows the length of the copper tab prior to the second layer being printed. As soon as infill of the second tab is complete on the first layer, a second copper tape tab is placed while the perimeter path is being printed on the second layer.

Below, Figure 18 shows the second layer being printed after the second electrode had been placed. After longitudinal infill was completed, each electromechanical sample underwent the same curing process described above in Section 3.2.

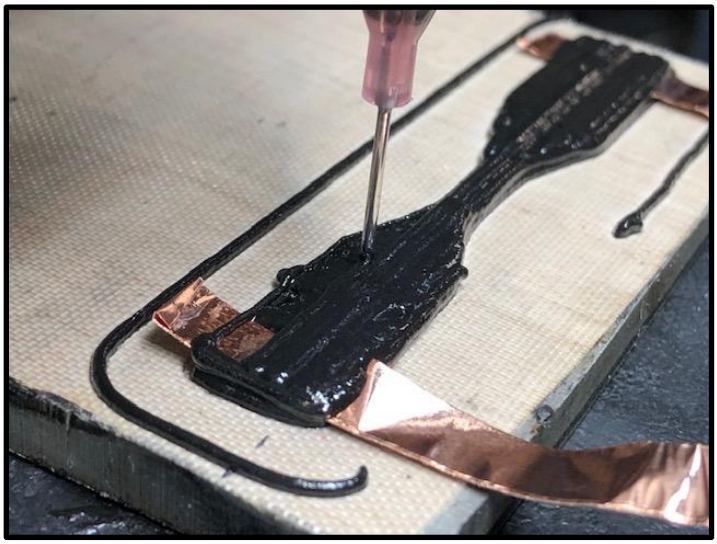

Figure 18: Second layer of conductivity dogbone being printed

Section 3.4: Proof of Concept

Before exploring the details of the characterization of the epoxies, it is important to illustrate the functionality of the shape memory epoxy. It was shown that with the integration of carbon black, MWCNTs, and VMX24 carbon short fiber, there was no detriment enforced on the shape memory properties of the base epoxy, Epon 862. Furthermore, the novel use of both Epikure W and Epikure 9553 curing agents did not hinder the shape memory functionality. Below, Figure 19 shows the model of a demonstration sample that was printed to illustrate the shape memory effect of the MWCNT-based epoxy. The model is designed to be a single layer print with the triangular tabs folded inward on top of one another.

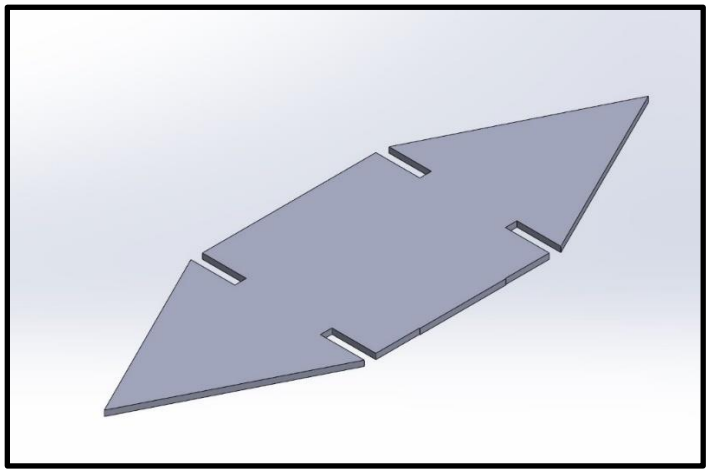

Figure 19: CAD model of shape memory demonstration print

After printing the geometry in Figure 19 above, an oil bath was heated on a hot plate and the printed component was submerged, increasing its temperature beyond the glass transition point. After achieving a sufficiently high temperature to allow the entire component to enter the amorphous, ductile phase, it was then manipulated into a folded

position. Figure 20 below illustrates that printed geometry with the triangular tabs folded inward after being immersed in the oil bath.

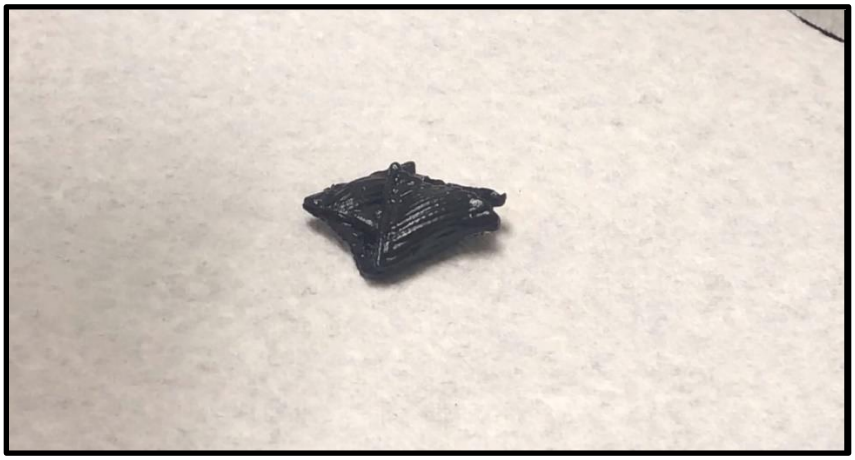

Figure 20: Folded MWCNT demonstration print

After folding and being allowed to cool in the folded position, the sample was then heated with a heat gun. As heat was induced, the sample's glass transition temperature was again exceeded, activating the shape memory function. Figure 21 below illustrates the various stages of deployment as the printed geometry continuously unfolded back into its original, printed form.

Figure 21: Unfolding process of MWCNT demonstration print

In addition to illustrating the retention of the shape memory effect for MWCNT-based inks, Figure 22 below also illustrates the model of a print used to demonstrate the effect for printed carbon black inks. This particular design was intended to be folded into

a box to illustrate the high recovery percentage of the ink. This print, like the one used for the MWCNT samples, was designed to be printed in a single layer.

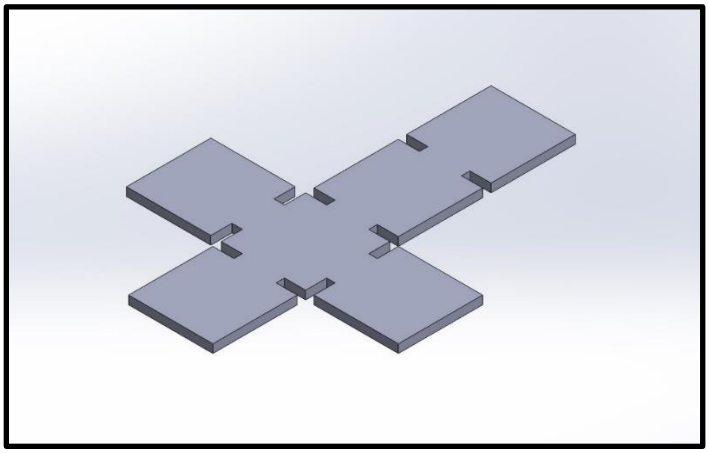

Figure 22: CAD model of second demonstration print

This sample was heated while being submerged in heated oil on a hot plate, similar to the process described for the MWCNT sample. After sufficient heating, it was folded into the box structure seen below in Figure 23.

Figure 23: Carbon black demonstration print folded into box

As the sample was heated with the heat gun, it began recovering from its temporary form to its printed structure. The recovery process can be seen below in Figure 24. It is

apparent through comparison between the final recovery image (d) and the model image in Figure 22 above that the recovery percentage, although not explicitly recorded, was high.

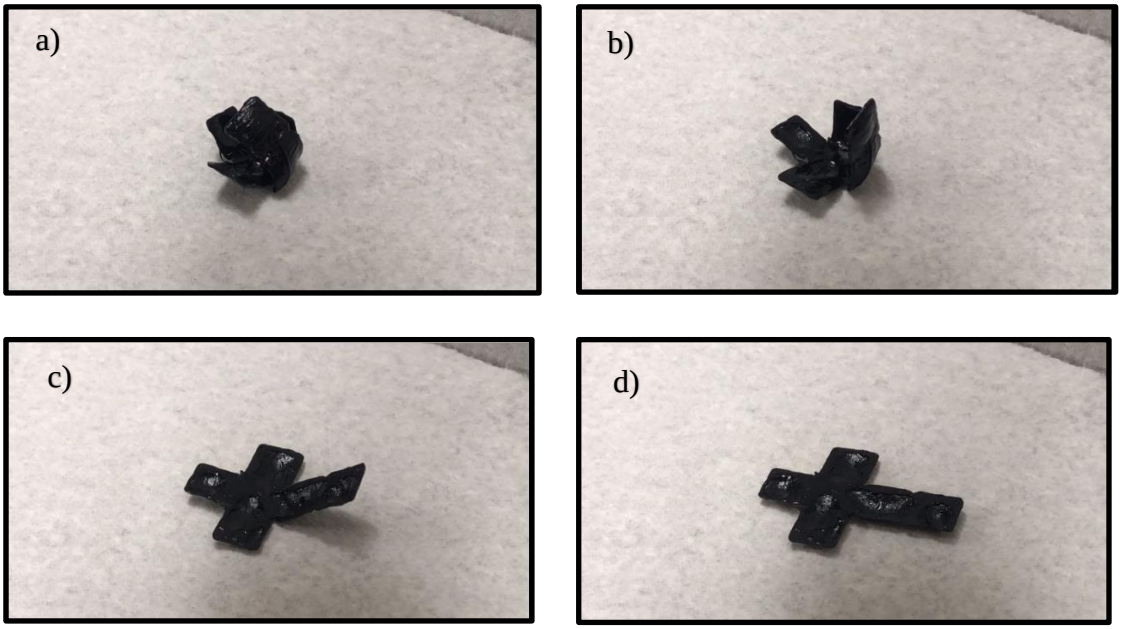

Figure 24: Unfolding process of carbon black demonstration print

Section 3.5: Experimental Setups

To study the mechanical performance of both carbon black- and MWCNT-based printed samples, the samples were placed in tensile jaws of an Instron 5969 and strained. The test profiles varied depending on the type of test being performed, but all numerical controls related to specimen strain rate and time spent at a given strain position were controlled by the Bluehill software. This software allowed for the Instron to be preprogrammed to apply strain indefinitely, in the case of tensile tests to failure, or to load repeatedly, in the case of cyclic loading trials.

The D638 Type V dogbone samples were tested at both elevated temperatures and room temperature. Testing at elevated temperatures was done at 110°C, a temperature

known to exceed the glass transition temperature of Epon 862 when combined with the two curing agents used. To achieve the desired thermal environment, a thermal chamber, which is mounted on the Instron's frame, is able to be rolled forward to totally enclose the atmosphere surrounding the test specimen in the jaws of the Instron.

The thermal chamber was controlled manually for all tests utilizing a control panel located on the chamber's external surface. However, when integrated with the desktop controlling the Instron, a more exact numerical control system can be utilized to precisely control temperature ramping procedures in accordance with the strain applied to the test specimen.

In addition to mechanical testing, certain test samples, like those shown above in Section 3.3, were used to monitor electromechanical response. For those tests, a cyclic loading test profile similar to the one described for the mechanical samples was utilized. This profile, however, limited strain to a much lower extent to prevent plastic deformation and cycled to peak strain only twice. During this cyclic loading, a datalogging instrument, in this case an Agilent 34401A, was utilized to monitor electrical continuity and resistance by placing the leads of the datalogger on both of the copper tape tabs described in Section 3.3. These tabs, again, were placed between the two layers of the print and were permanently embedded in the print following the curing process.

CHAPTER 4: RESULTS AND ANALYSIS OF PRINTED SAMPLES

Section 4.1: Print Accuracy

Beginning with an analysis of the quality and consistency of the printed D638 Type V dogbones, Figure 25 below shows the average test section thicknesses and widths for carbon black based epoxy prints from 1 wt% to 3 wt% VMX24 short fiber. These measurements were taken with Fowler digital calipers with a least count of 0.01mm. The averages shown were derived from four test samples of each short fiber concentration prior to any mechanical characterization.

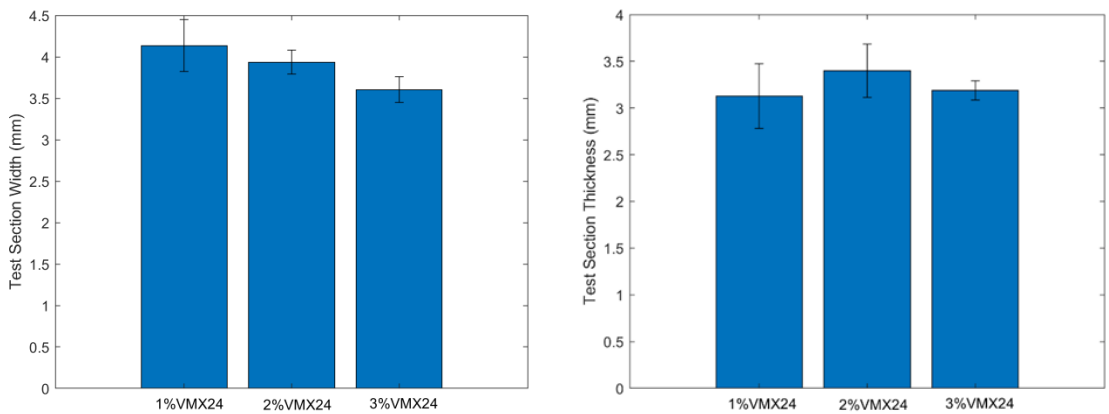

Figure 25: Average test section widths and thicknesses for carbon black samples

The data shown above in Figure 25 is shown below in Table 1 with the quantification of the error bars and average dimensional values.

Table 1: 10 wt% Carbon black average test section dimensions by short fiber content

Print Sample	Average Test Width (mm)	Average Test Height (mm)
1 wt% VMX24	4.135 ± 0.313	3.128 ± 0.345
2 wt% VMX24	3.935 ± 0.145	3.398 ± 0.284
3 wt% VMX24	3.605 ± 0.154	3.188 ± 0.104

From this information, the printing accuracy for the carbon black based inks was verified, with the only significant trend coming in the average test widths. As short fiber concentration increased, the average test width decreased, likely the result of increased yield stress in the higher fiber containing inks. Also, it is apparent that relative to the dogbone model, the test thicknesses are much closer on average to the theoretical dimension than are the test section widths.

Similarly, analyzing the MWCNT inks, Figure 26 below shows the average test section thicknesses and widths for MWCNT prints ranging from 0 wt% to 7.5 wt% VMX24 short fiber. The averages shown were derived from three test samples of each short fiber concentration prior to any mechanical characterization.

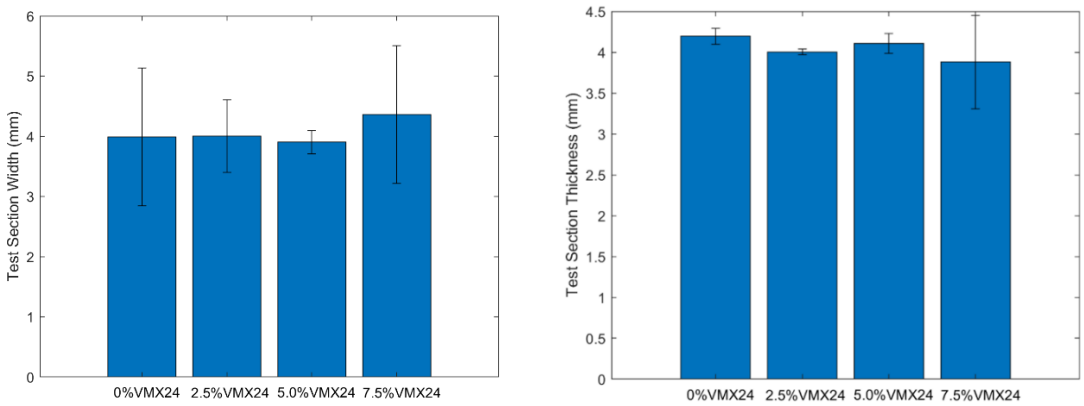

Figure 26: Average test section widths and thicknesses for MWCNT samples

Again, the data shown above is quantified below in Table 2, where the error bars are quantified in a table format. In this case, the prints varied equally in test width and test thickness, with no apparent trend related to short fiber content.

Table 2: 1.5 wt% CNT average test section dimensions by short fiber content

Print Sample	Average Test Width (mm)	Average Test Height (mm)
0 wt% VMX24	3.990 ± 1.144	4.195 ± 0.095
2.5 wt% VMX24	4.005 ± 0.603	4.055 ± 0.031
5.0 wt% VMX24	3.903 ± 0.193	4.107 ± 0.123
7.5 wt% VMX24	4.260 ± 1.144	3.880 ± 0.572

While the averages are relatively consistent, compared to the carbon black samples the MWCNT-based ink presents larger error in the width with sufficiently low error in the thicknesses, which is primarily the result of a higher standard deviation in the widths and a relatively low sample size.

Section 4.2: Tensile Tests – Carbon Black Non-Degassed

Above, Section 3.2 describes a specific mixing process including the degassing of the composite ink prior to the beginning of the printing process. However, a series of print samples and tensile tests were performed without degassing the ink prior to printing, allowing for the correlation of porosity effects to the mechanical performance of the samples. Below, Figure 27 shows a strain-to-failure test done at room temperature with non-degassed samples composed of 10 wt% carbon black at 1, 2, and 3 wt% VMX24 short fiber concentrations. Without degassing, the resulting trend, when analyzing only ultimate tensile strengths, is suspect. The elastic moduli of the 1, 2, and 3 wt% short fiber samples

generally increased with higher concentrations of short fiber, with the 2 and 3 wt% samples having similar moduli. However, the 1, 2, and 3 wt% short fiber samples had ultimate tensile strengths that varied, not following a linear increase with short fiber concentration.

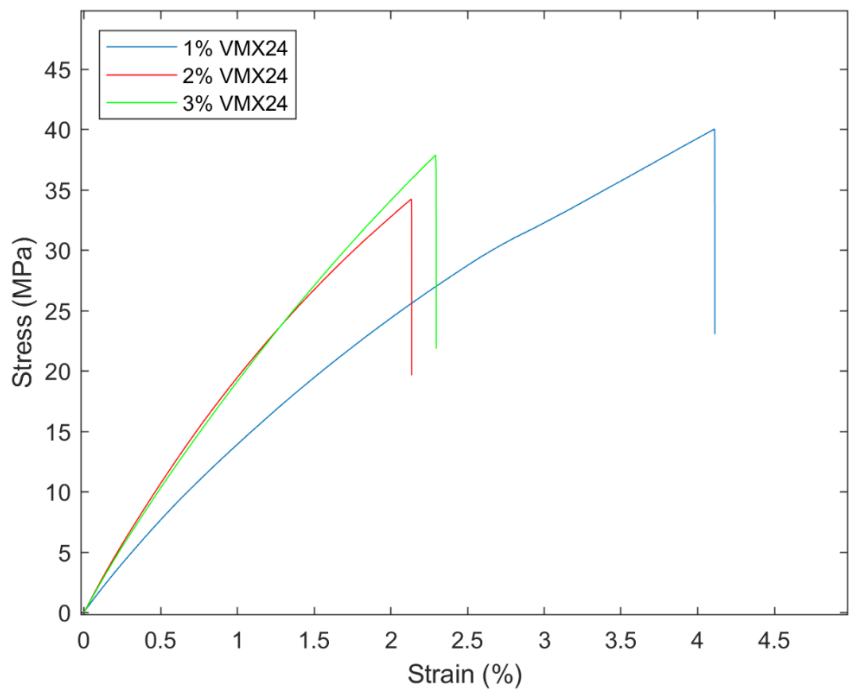

Figure 27: Room temperature strain-to-failure trials for non-degassed 10 wt% carbon black, short fiber prints

According to other works where similar composites were cast rather than printed, the trend would typically follow a pattern of increasing modulus and ultimate tensile strength with increasing short fiber concentration. The elastic moduli and ultimate tensile strengths of the strain-to-failure trials from Figure 27 are shown below in Table 3.

Table 3: Results of 1st room temperature, degassed, carbon black, short fiber trials

Print Sample	**Modulus of Elasticity, E (MPa)**	**Ultimate Tensile Strength, σ_{max} (MPa)**
1 wt% VMX24	17.25	40.03
2 wt% VMX24	23.65	34.23
3 wt% VMX24	22.70	37.89

Upon examination with a microscope, all three samples were found to have excessive porosity within the cross section of the fracture area in the test region of the sample. The stress concentrations resulting from the pronounced porosity, assumed to be the result of the mixing process, clearly had a dominating effect on the ultimate tensile strengths of the samples. Below, Figures 28, 29, and 30 show the three specimen cross sections from Figure 27.

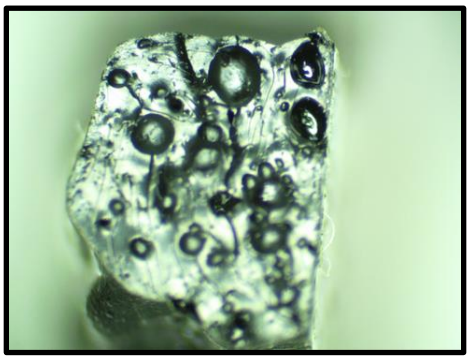

Figure 28: Cross section of non-degassed 10 wt% carbon black, 1 wt% short fiber print

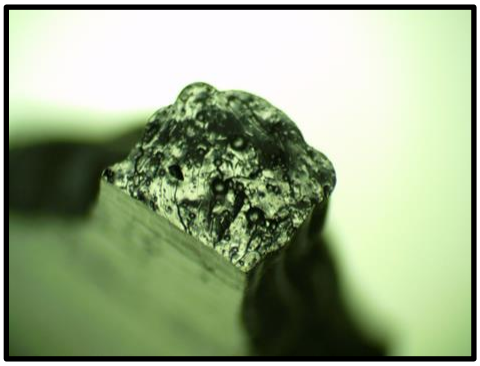

Figure 29: Cross section of non-degassed 10 wt% carbon black, 2 wt% short fiber print

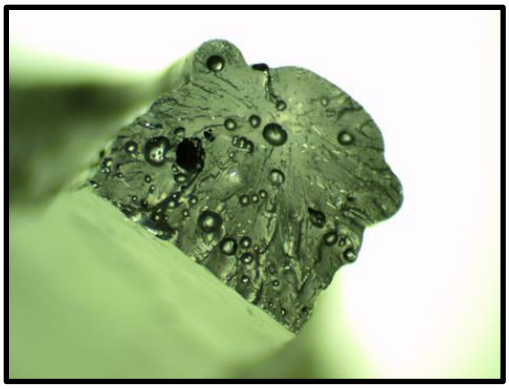

Figure 30: Cross section of non-degassed 10 wt% carbon black, 3 wt% short fiber print

Given the likelihood of all non-degassed samples being mechanically flawed or structurally unsound, the test from Figure 27 was repeated with three new samples of the same short fiber and carbon black content. Although these porosity characteristics may be equal among all samples whose ink was prepared in the same manner, the results needed to be confirmed before assumptions about porosity consistency could be made. The results of that confirmation test are shown below in Figure 31. Again, an unreasonable distribution of ultimate tensile strengths was seen among the three samples with equally suspect distribution of the moduli. For this test, the ultimate tensile strengths of the 1 and 3 wt% samples were not replicated from the first trial, while the ultimate tensile strength of the 2 wt% sample was virtually unchanged. The same could be said for the distribution of moduli, where the lower short fiber concentrations yielded a much different modulus from the first trial. Again, the modulus of the 3 wt% sample was replicated from the first trial.

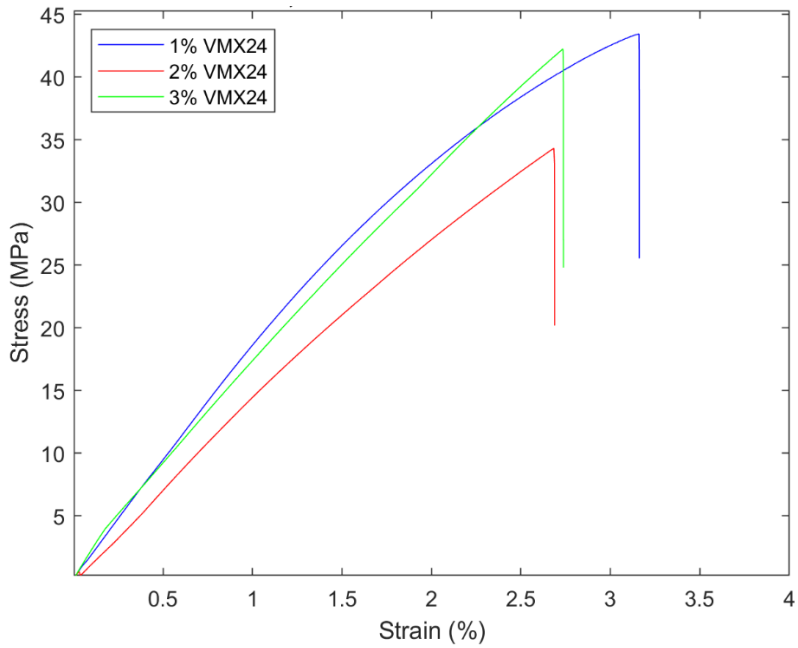

Figure 31: 2nd room temperature strain-to-failure trials for non-degassed 10 wt% carbon black, short fiber prints

The moduli and ultimate tensile strengths of the second room temperature trial are shown below in Table 4.

Table 4: Results of 2nd room temperature, non-degassed, carbon black, short fiber trials

Print Sample	**Modulus of Elasticity, E (MPa)**	**Ultimate Tensile Strength, σ_{max} (MPa)**
1 wt% VMX24	19.41	43.47
2 wt% VMX24	11.56	34.34
3 wt% VMX24	23.24	42.27

These results imply an 8.6% increase in ultimate tensile strength of the 1 wt% short fiber sample and an 10.4% increase in ultimate tensile strength of the 3 wt% short fiber sample. The ultimate strains varied significantly as well as can be seen in Figures 27 and 31. These variations in strain and stress were questionable, which therefore indicated that an underlying structural difference may be at fault.

Upon examination with a microscope, all three samples were again found to have excessive porosity within the cross section of the fracture area in the test region of the sample. This porosity is assumed to be the dominating driver behind the varied ultimate tensile strengths and moduli between both the original and the confirmation tensile trials. Below, Figures 32, 33, and 34 show the three specimen's cross sections from Figure 31.

Figure 32: Cross section of non-degassed 10 wt% carbon black, 1 wt% short fiber print

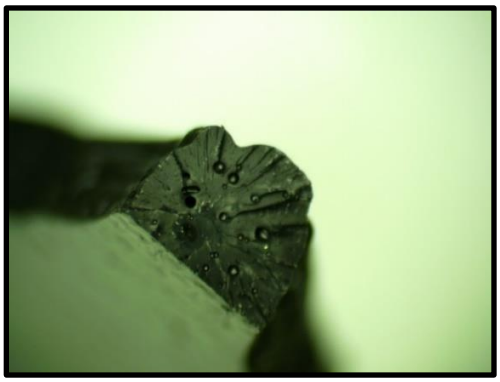

Figure 33: Cross section of non-degassed 10 wt% carbon black, 2 wt% short fiber print

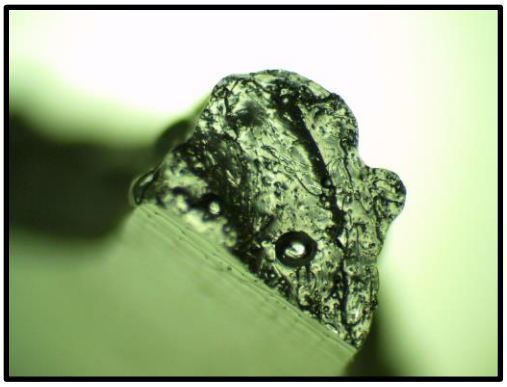

Figure 34: Cross section of non-degassed 10 wt% carbon black, 3 wt% short fiber print

In addition to conducting tensile tests to failure at room temperature, following the first trails at room temperature, samples printed with the same carbon black and VMX24 short fiber content and same preparation process were tested at elevated temperatures. These tests helped to determine the behavior of the composite prints in their amorphous state. After multiple shape memory effect verification exercises, where the printed components exhibited shape memory and reassumed their original crystalline structure after amorphous deformation, the apparent glass transition temperature was around 100°C. For that reason, this high temperature strain-to-failure test was performed at 110°C. The results of the elevated temperature strain-to-failure test is shown below in Figure 35. For this test, the ultimate tensile strengths of the 1, 2, and 3 wt% short fiber samples were 3.74 MPa, 4.76 MPa, and 5.35 MPa respectively.

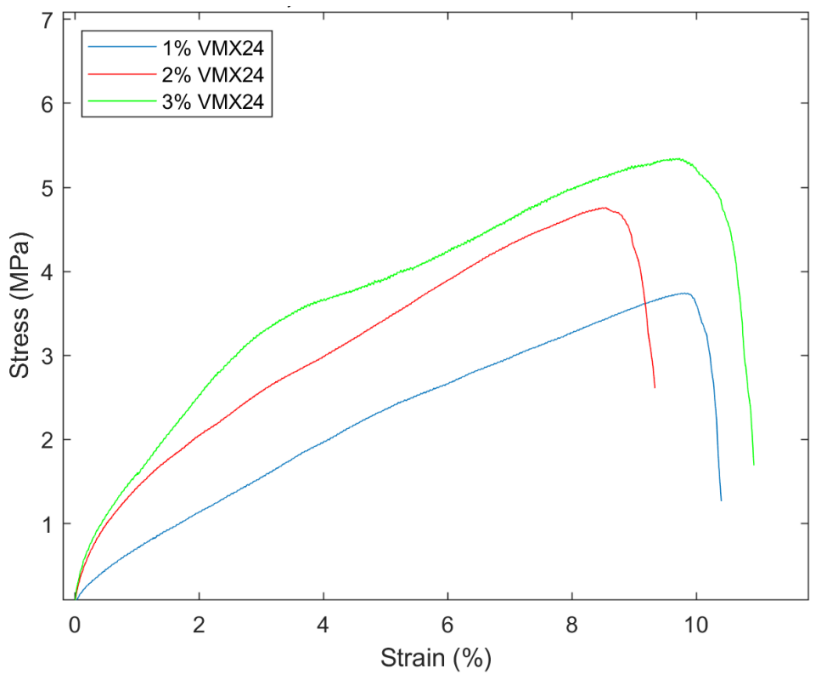

Figure 35: High temperature strain-to-failure trials for non-degassed 10 wt% carbon black, short fiber prints

Section 4.3: Tensile Tests – Carbon Black Degassed

Upon examination of the non-degassed test samples and the results of the tensile tests that followed, an array of the same dogbones were printed following the degassing mixing procedures laid out in Section 3.2. Again, this tensile test was conducted at room temperature, straining the samples to failure. For this test, the ultimate tensile strengths of the 1, 2, and 3 wt% short fiber samples were more consistent and were distinctly higher than the non-degassed counterparts. Below, Figure 36 shows those results and the well-behaved trend of increasing fracture stress with increasing short fiber content.

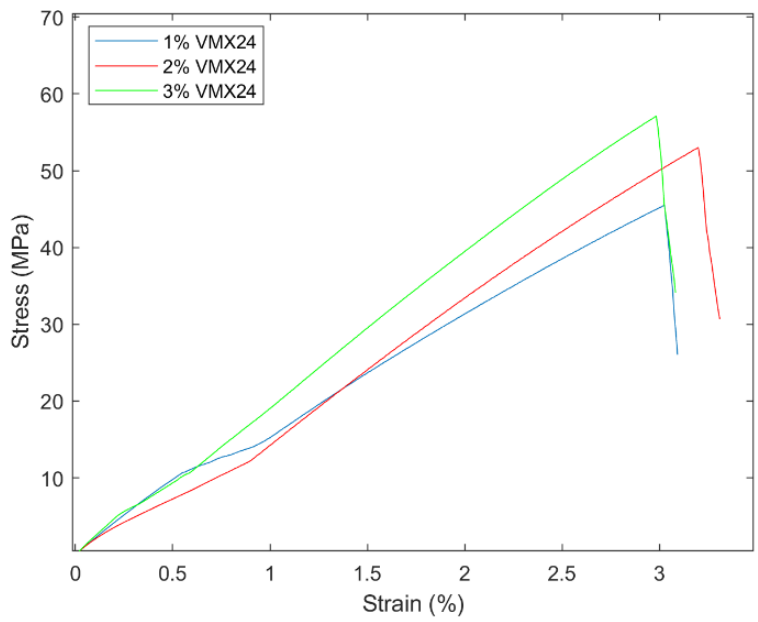

Figure 36: Room temperature strain-to-failure trials for degassed 10 wt% carbon black, short fiber prints

The moduli and ultimate tensile strengths of the room temperature trials of degassed samples are shown below in Table 5.

Table 5: Results of room temperature, degassed, carbon black and short fiber trials

Print Sample	**Modulus of Elasticity, E (MPa)**	**Ultimate Tensile Strength, σ_{max} (MPa)**
1 wt% VMX24	21.05	45.51
2 wt% VMX24	18.40	53.03
3 wt% VMX24	23.51	57.12

These results much more closely resembled what was expected for the increased loading of short fibers. These results also imply a 4.7% increase, 54.4% increase, and a 35.1% increase in ultimate tensile strength for 1, 2, and 3 wt% short fiber samples respectively when compared to the highest fracture stresses of the non-degassed counterparts of the previous two room temperature trials of Section 4.2. It is important to note that the 3 wt% sample had a modulus very similar to that of both non-degassed 3 wt%

samples. While there is an obvious difference in the fracture stress of the degassed and non-degassed 3 wt% samples, it appears that perhaps at high loadings of short fiber, degassing has diminished effects on the elastic modulus. Also, the elastic moduli of the 1 and 2 wt% samples experienced an obvious benefit from the degassing process.

Further validating the data from Figure 36 and Table 5 above, qualitative analysis, again examining the cross section of the fractured test section, was obtained through microscope images. Those images are shown below in Figures 37, 38, and 39. Clearly, the degassing of the mixed ink prior to the printing process was effective in removing the macro-porosity, helping to regulate the results from the tensile tests that yielded more consistent results.

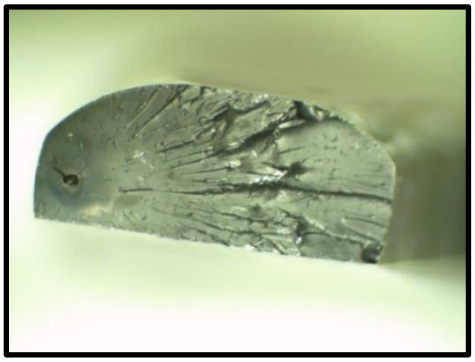

Figure 37: Cross section of degassed 10 wt% carbon black, 1 wt% short fiber print

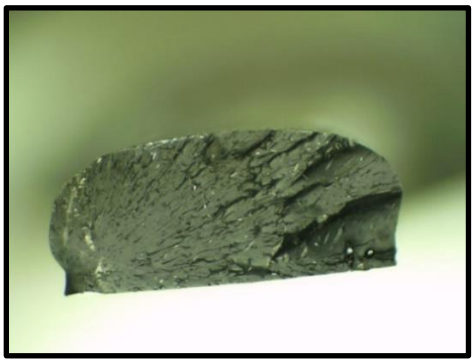

Figure 38: Cross section of degassed 10 wt% carbon black, 2 wt% short fiber print

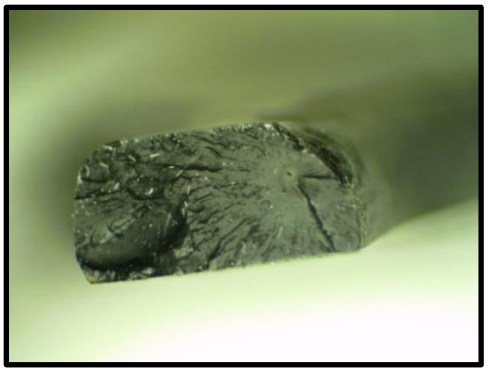

Figure 39: Cross section of degassed 10 wt% carbon black, 3 wt% short fiber print

Additionally, just as for the non-degassed samples, a high temperature strain-to-failure test was also performed for degassed prints of the same composition as the preceding room temperature trials. For this test, shown below in Figure 40, the same test procedure for Figure 35 was utilized. The ultimate tensile strengths of the degassed 1, 2, and 3 wt% short fiber samples were 4.44 MPa, 6.70 MPa, and 8.45 MPa respectively, showing a marked increase in strength for all three samples when compared to their non-degassed counterparts.

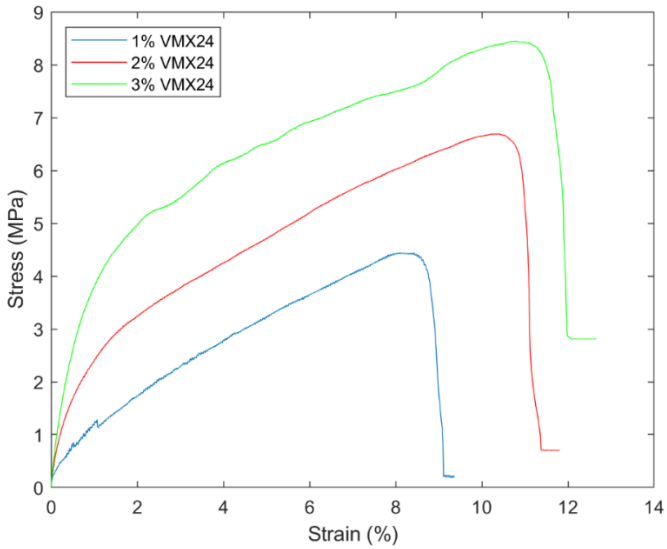

Figure 40: High temperature strain-to-failure trials for degassed 10 wt% carbon black, short fiber prints

Below, Figure 41 shows all of the room temperature fracture data for degassed and non-degassed samples, illustrating the effects of the degassing process. The degassed samples are denoted by a solid line and defined by the legend as degassed. In all degassed samples, the ultimate tensile strength was higher than both of the non-degassed counterparts for that given short fiber loading.

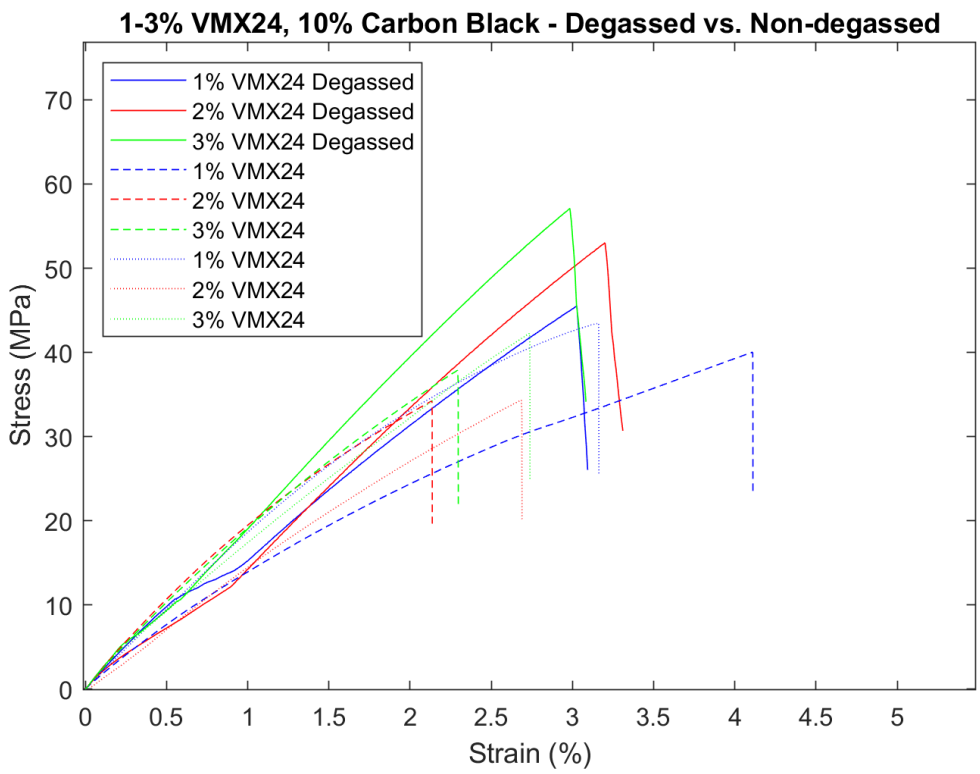

Figure 41: Strain-to-failure trials of degassed and non-degassed 10 wt% carbon black, short fiber prints

In addition to testing degassed and non-degassed specimens to failure, degassed samples were also tested cyclically at high temperature to monitor the reduction in maximum stress per cycle. Below, Figure 42 shows the results of that test, where each specimen was loaded at 0.5% strain in a thermal chamber set to 110°C. The loading to the

0.5% strain position relative to the initial position was cycled 6 times for each specimen, with each loading cycle experiencing a reduction in the maximum stress seen.

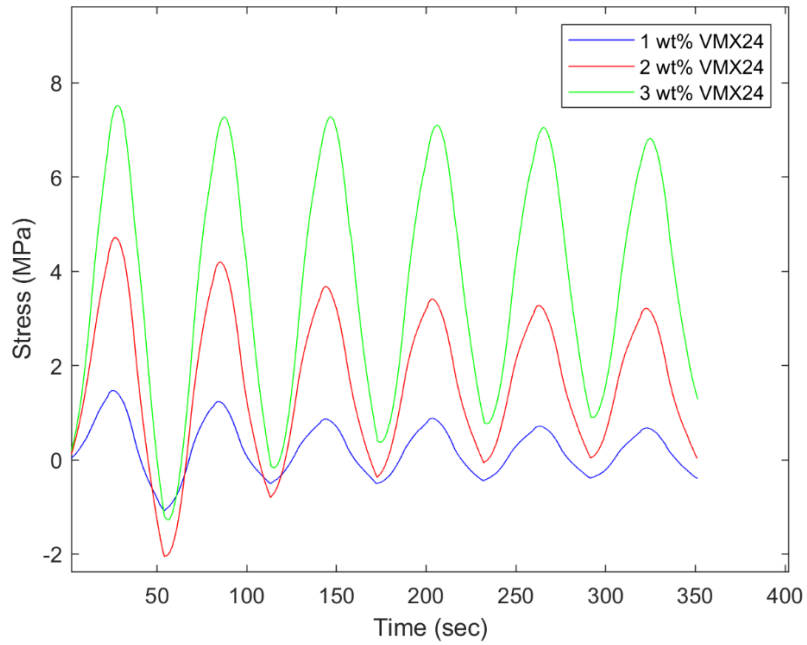

Figure 42: High temperature cyclic loading of 10 wt% carbon black, short fiber prints

The results from Figure 42 above have been arranged below in Table 6, which lists the maximum stress for each of the 6 cycles endured by each sample. The maximum stress for each sample, as expected, decreased with each loading cycle, indicating a fundamental degradation of the print's structural integrity with each strain cycle.

Table 6: Maximum stress for each loading cycle of high temperature strain trials

Cycle #	**1 wt% VMX24**	**2 wt% VMX24**	**3 wt% VMX24**
1	1.45 MPa	4.63 MPa	7.39 MPa
2	1.21 MPa	4.13 MPa	7.20 MPa
3	0.85 MPa	3.67 MPa	7.20 MPa
4	0.87 MPa	3.37 MPa	6.98 MPa
5	0.71 MPa	3.22 MPa	6.98 MPa
6	0.66 MPa	3.22 MPa	6.79 MPa

While the trend in maximum stress is obvious, it is also noteworthy the amount by which the maximum stress decreased each cycle. The difference between the maximum stress for a given cycle and the preceding cycle is shown below in Table 7. The average stress reduction per cycle for the 1, 2, and 3 wt% short fiber samples was 0.159 MPa, 0.282 MPa, and 0.118 MPa respectively.

Table 7: Stress reduction per cycle of high temperature strain cycles

Cycle #	1 wt% VMX24	2 wt% VMX24	3 wt% VMX24
2	0.248 MPa	0.502 MPa	0.183 MPa
3	0.357 MPa	0.453 MPa	0.002 MPa
4	0.024 MPa	0.304 MPa	0.217 MPa
5	0.165 MPa	0.150 MPa	0.003 MPa
6	0.048 MPa	0.001 MPa	0.185 MPa

Section 4.4: Carbon Black - Resistance Tests

In addition to exploring the mechanical characteristics of the carbon black and short fiber samples, the electromechanical response was also analyzed. By analyzing the change in resistance resulting from physical strain, the potential for this composite epoxy to be used as a strain sensor can be investigated. For these tests, the two-layer samples with copper tape electrodes protruding from the grip tabs were strained to 0.5% while continuous current was applied to the sample through the electrodes.

Below, Figure 43 shows the resistance response profile for two strain cycles performed on printed samples composed of 10 wt% carbon black and 1 wt% VMX24 short fiber. Between the two trials, the average range in resistance throughout the loading cycle was 512.8 Ohms, with resistance maximums occurring at the apex of the strain cycle and

the minimums occurring when the jaws had fully relaxed the sample back to the neutral position following the first loading cycle.

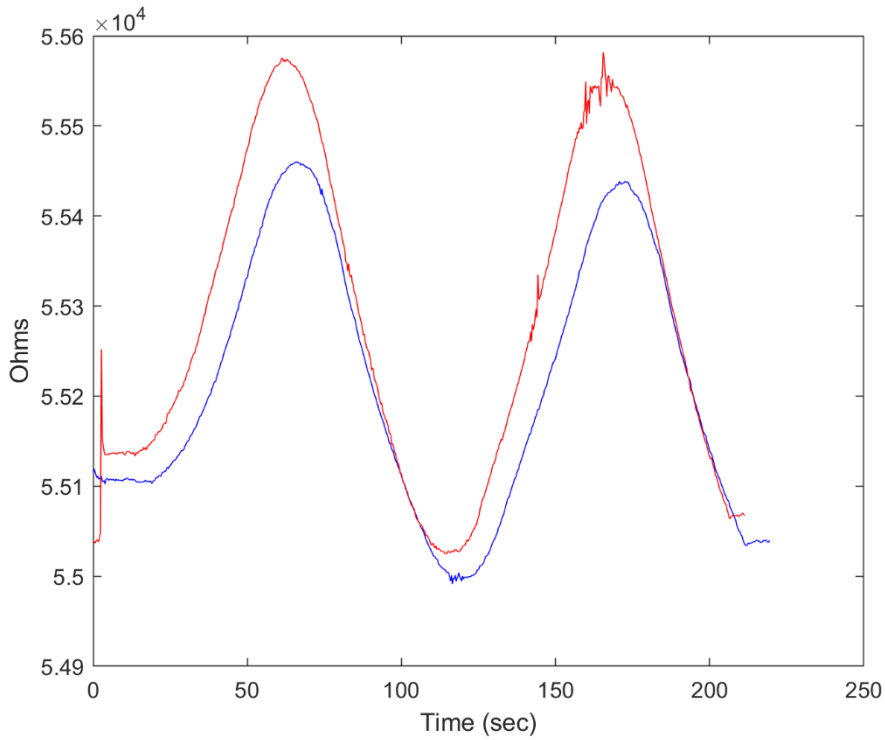

Figure 43: Strain-resistance profile for 10 wt% carbon black, 1 wt% short fiber

Figure 44 below shows the resistance response profile for three strain cycles performed on printed samples composed of 10 wt% carbon black and 2 wt% VMX24 short fiber. Between the three trials, the average range in resistance throughout the loading cycle was 326.3 Ohms. Again, the resistance maximums occurred at the apex of the strain cycle and the minimums occurred when the jaws had fully relaxed the sample back to the neutral position following the first loading cycle.

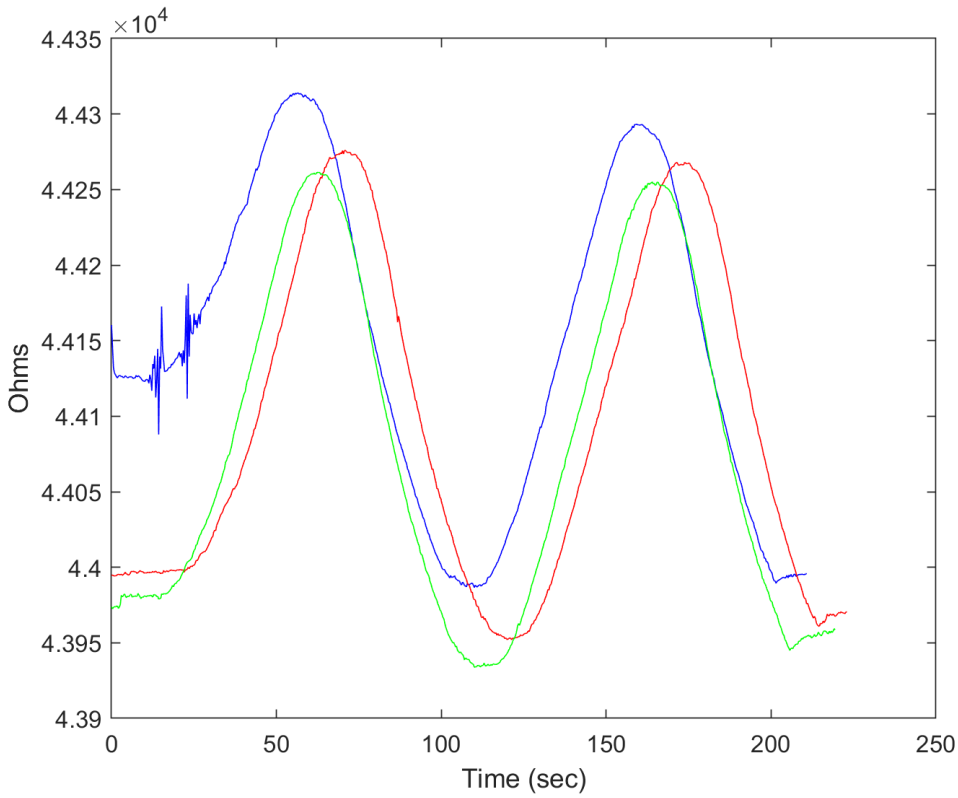

Figure 44: Strain-resistance profile for 10 wt% carbon black, 2 wt% short fiber

Below, Figure 45 shows the resistance response profile for three strain cycles performed on printed samples composed of 10 wt% carbon black and 3 wt% VMX24 short fiber. Between the three trials, the average range in resistance throughout the loading cycle was 293.8 Ohms. Again, the resistance maximums occurred at the apex of the strain cycle and the minimums occurred when the jaws had fully relaxed the sample back to the neutral position following the first loading cycle.

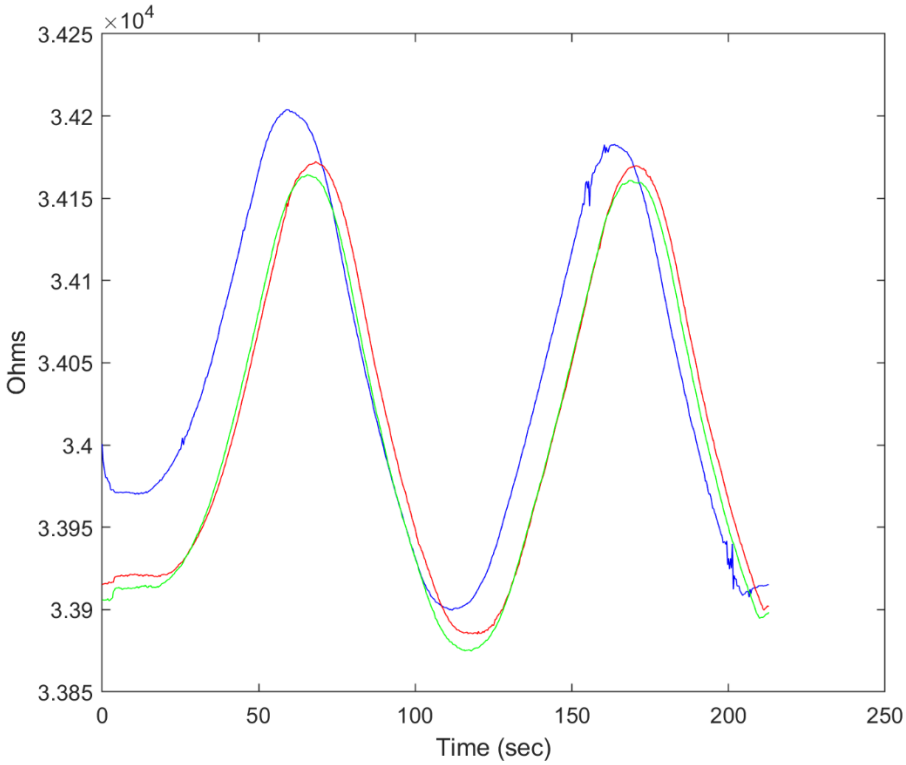

Figure 45: Strain-resistance profile for 10 wt% carbon black, 3 wt% short fiber

Below, Figure 46 shows the average initial resistances and resistance response from 0.5% strain for the carbon black samples shown above in Figures 43, 44, and 45. The trend is clear, showing lower initial resistance and electromechanical response with increased short fiber content, indicating that lower short fiber loading would yield more highly responsive sensors.

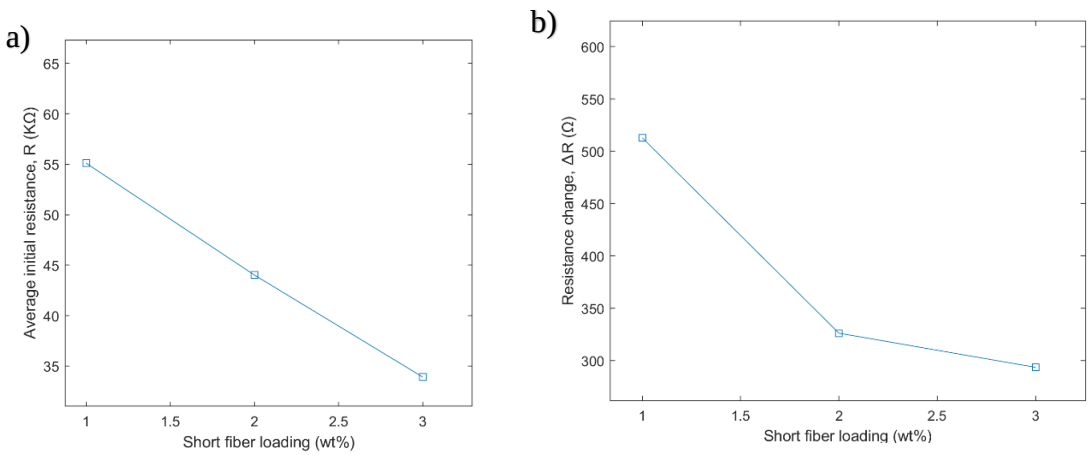

Figure 46: Initial resistance (a) and resistance response by short fiber loading (b)

Below, Table 8 gathers the average resistance ranges for each of the three short fiber loadings.

Table 8: Resistances by short fiber content of strained 10 wt% carbon black prints

Short Fiber Loading	**Average Initial Resistance (KΩ)**	**Average Resistance Range (ΔΩ)**
1 wt%	55.11	512.8
2 wt%	44.03	326.3
3 wt%	33.93	293.8

Given that the same test profile and strain rate was utilized for all three short fiber loadings, the three plots can be shown on the same diagram to illustrate the resistance of each short fiber concentration relative to one another. Since for each set of trials, the resistance response was repeatable, only one of the strain loading cycles is shown for each of the three short fiber concentrations used. Shown below in Figure 47, each of the three short fiber concentrations are represented. The average resistance of the 1, 2, and 3 wt% short fiber samples shown were 55.25 kΩ, 44.12 kΩ, and 34.02 kΩ respectively, illustrating a clear reduction in resistance with increasing loading of the VMX24 short fiber.

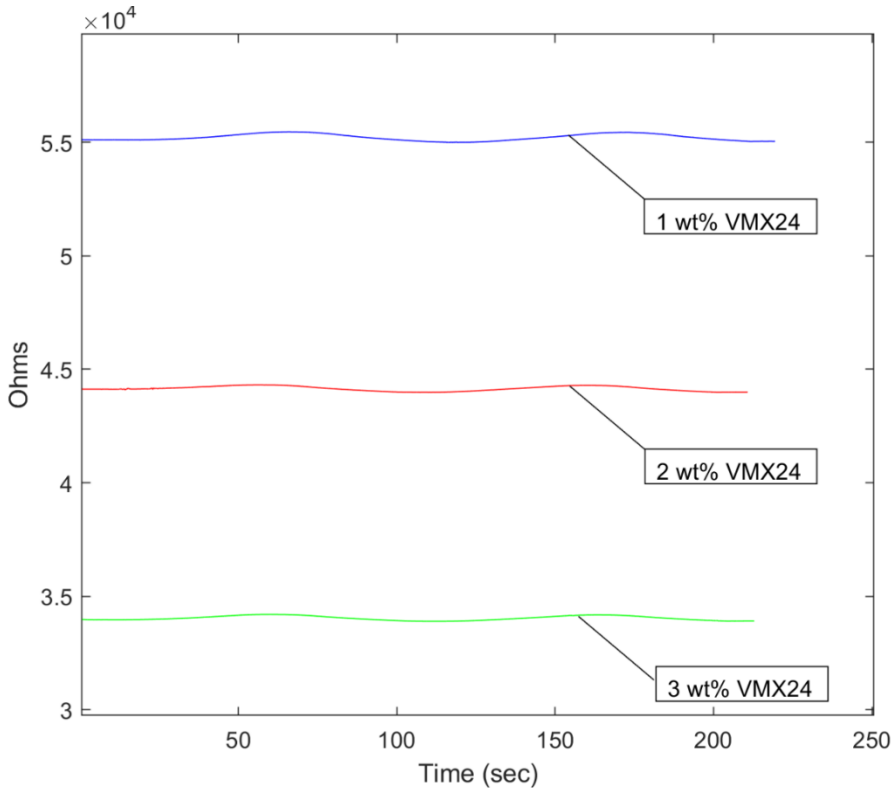

Figure 47: Resistance profiles of 10 wt% carbon black, 1-3 wt% short fiber prints

Section 4.5: Tensile Tests – MWCNT

For the second major area of focus, the MWCNT-based printed epoxy samples were also tested to failure in a similar manner to the carbon black-based samples. The MWCNT-supported epoxy components printed with 0, 2.5, 5.0, and 7.5 wt% VMX24 short fiber were tested with the same test profile described for the carbon black-based samples of Section 4.2 and Section 4.3. The results of these trials are shown below in Figure 48. These strain-to-failure trials were performed at room temperature and the samples, like the first carbon black trials shown in Section 4.2, did not undergo a degassing procedure prior to printing.

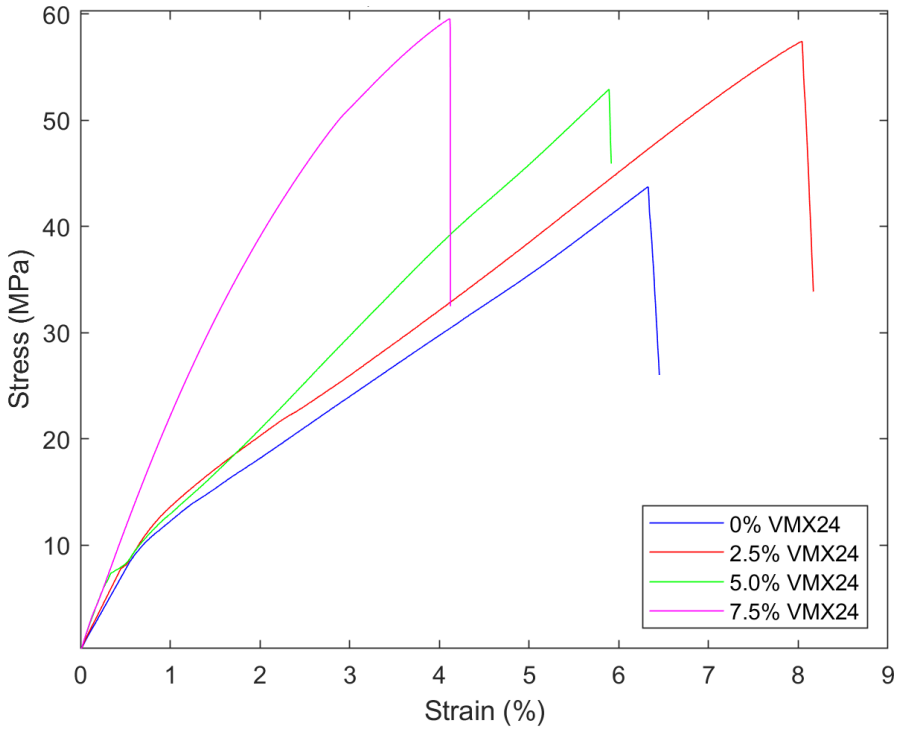

Figure 48: Strain-to-failure trials for 1.5 wt% MWCNTs, 0-7.5 wt% short fiber prints

The moduli and ultimate tensile strengths of the MWCNT prints tested in Figure 48 are shown below in Table 9.

Table 9: Results of room temperature, 1.5 wt% MWCNT strain-to-failure trials

Print Sample	**Modulus of Elasticity, E (MPa)**	**Ultimate Tensile Strength, σ_{max} (MPa)**
0 wt% VMX24	17.27	43.75
2.5 wt% VMX24	19.42	57.45
5.0 wt% VMX24	25.50	52.94
7.5 wt% VMX24	26.13	59.56

The ultimate tensile strengths perform as expected, with higher short fiber loadings possessing a higher fracture strength and elastic modulus, with the exception of the 2.5

wt% short fiber sample, which exceeded the 5.0 wt% sample in ultimate strength. Again, with higher short fiber loading, the maximum strain also decreased significantly except for in the case of the 2.5 wt% short fiber sample. Disregarding the 2.5 wt% sample, increasing short fiber content increased the modulus and ultimate tensile strength, while reducing ultimate tensile strain.

In addition to quantitative testing, for the MWCNT-based samples, qualitative information was also obtained through the use of microscope imaging. These images taken on the fracture surface revealed, although to only relatively slight severity, macro-porosity in both the 0 wt% and 2.5 wt% VMX24 short fiber samples. Those images are shown below in Figure 49.

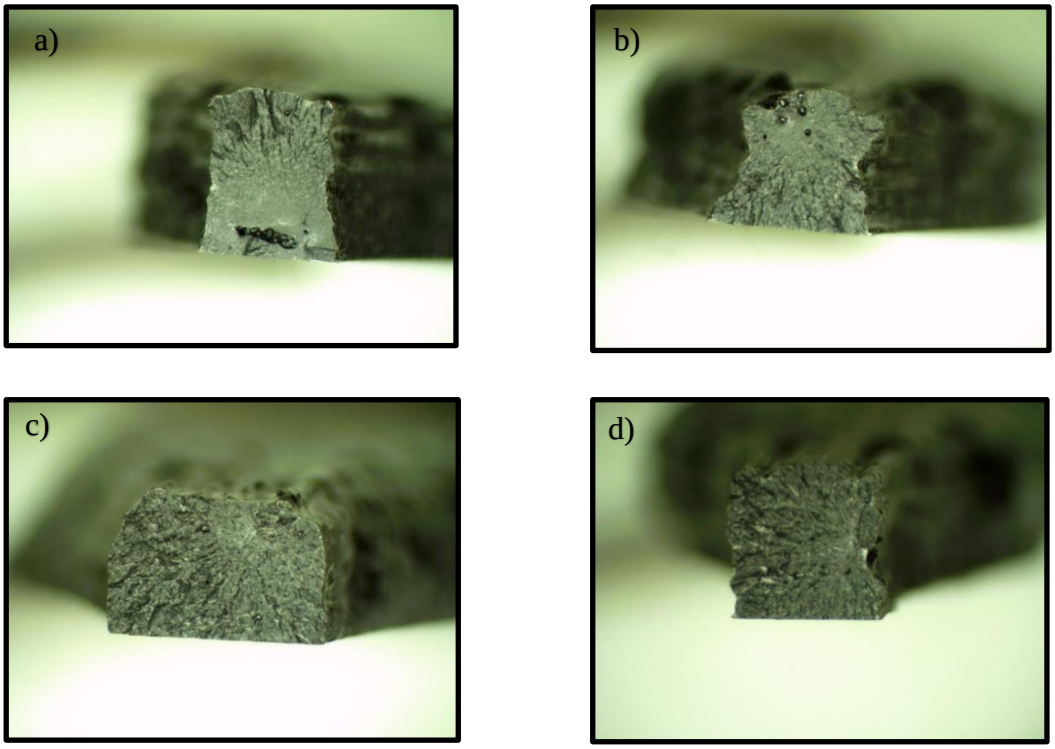

Figure 49: 1.5% MWCNT, 0(a), 2.5(b), 5.0(c), and 7.5 wt%(d) short fiber prints

Section 4.6: Thermal Cyclic Testing of MWCNT samples

Unique to the 1.5 wt% MWCNT samples, tensile loading was conducted before achieving failure. This loading was done cyclically, also introducing a thermal element in order to characterize the stress response during the transition from the crystalline to the amorphous stage. The results of the thermal cyclic trials are shown below in Figure 50. The maximum strain during the cyclic loading process was 0.5%. After the 0.5% strain was achieved at room temperature, the thermal chamber was activated, ramping the temperature to 110°C over the course of 3 minutes while strain was maintained. During that duration, stress fell for each sample. At the end of the heating period, the sample was relaxed to zero strain while being maintained at 110°C. Once the zero strain position was achieved, the thermal chamber was then opened and the sample was allowed to cool, over which period the stress again increased for each sample.

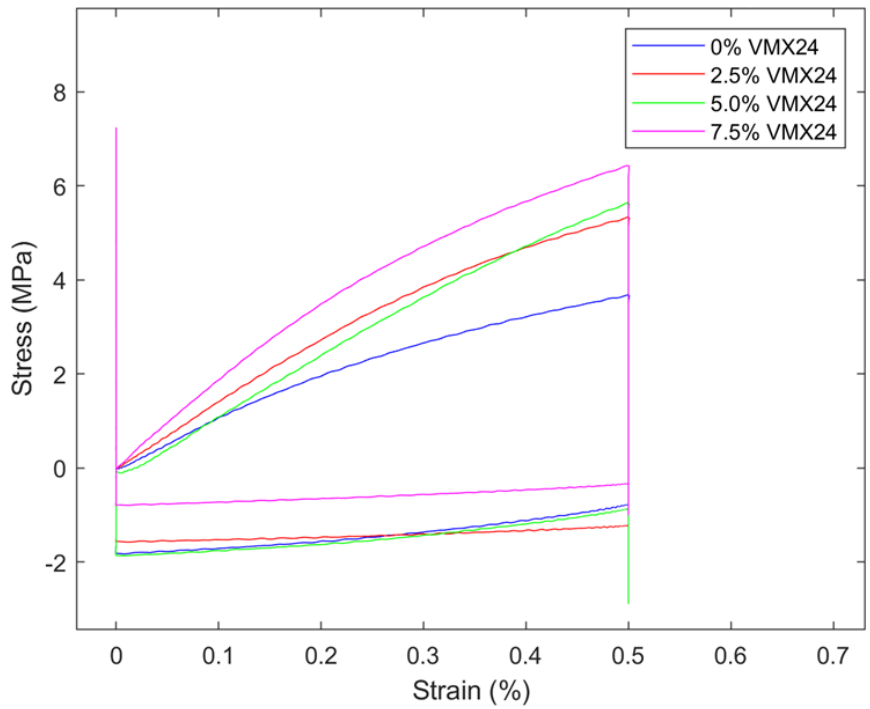

Figure 50: Thermal cyclic stress-strain curves of 1.5 wt% MWCNTs, short fiber prints

Below, Figure 51 shows the same stress data regarding the thermal cyclic trials performed on the MWCNT samples. However, on Figure 51, the x-axis is time, rather than strain, to better illustrate the stress progression throughout the test cycle.

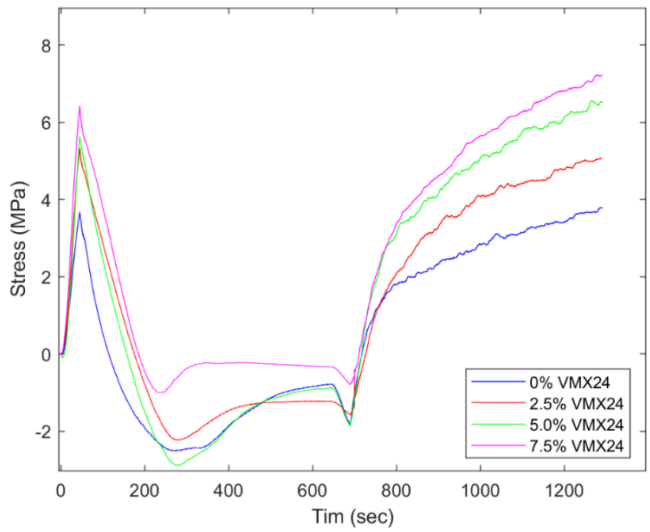

Figure 51: Thermal cyclic stress-time curves of 1.5 wt% MWCNTs, short fiber prints

From the trials illustrated in Figures 50 and 51, the stresses at 0.5% strain at room temperature for the 0, 2.5, 5.0, and 7.5 wt% VMX24 short fiber samples increased with short fiber content. With the exception of the 7.5 wt% sample, the magnitude of stress reduction during the heating cycle, $\Delta\sigma$, also increased with short fiber content, indicating that ductility in the amorphous phase could increase with the presence of a higher volume fraction of short fibers. Additionally, at the commencement of the cooling period to end the trials, the final stress, σ_f, increased with short fiber content, in all cases except for the 2.5 wt% sample exceeding the stress initially applied at 0.5% strain while at room temperature prior to the heating process. The thermal cyclic results are arranged below in Table 10.

Table 10: Tensile stress throughout thermal cyclic trials

Print Sample	**Stress at Initial Strain, $\sigma_{\varepsilon_{0.5},T_{rm}}$ (MPa)**	**Stress Reduction After Heating, $\Delta\sigma$ (MPa)**	**Stress After Cooling, σ_f (MPa)**
0 wt% VMX24	3.61	6.10	3.77
2.5 wt% VMX24	5.33	7.55	5.06
5.0 wt% VMX24	5.60	8.47	6.51
7.5 wt% VMX24	6.37	7.41	7.20

CHAPTER 5: CONCLUSIONS AND FUTURE WORK

Given the preceding information, there are clear impacts on the mechanical performance of the carbon black printed samples when a degassing process was utilized prior to printing. In addition to increasing the ultimate tensile strength for each short fiber loading, the carbon black samples that were degassed featured a higher modulus than their non-degassed counterparts. Also, the qualitative analysis confirmed that the degassing protocol was effective in reducing porosity when examining the cross sections of the fractured test samples. Given the cyclic loading trials, the carbon black samples also showed resilience when repeatedly strained in high temperature environments, seeing relatively low stress reduction per cycle and no trend in strength degradation relative to short fiber content. The carbon black epoxies also showed promise given their electromechanical response, where resistance response to strain was high and tunable by varying short fiber content, making this material a strong candidate as a sensing element.

Additionally, the MWCNT-based prints, although only characterized mechanically, showed good receptivity to the incorporation of carbon short fibers. For the room temperature strain-to-failure trials, the results consistently uncovered a higher modulus for increasing short fiber content, along with ultimate tensile strengths which increased linearly with short fiber content apart from the 2.5 wt% short fiber sample. The thermal cyclic trials, too, showed consistently increasing stress at the 0.5% strain position for increasing short fiber content. Apart from the 7.5 wt% short fiber sample, the stress reduction during the heating process also increased consistently with increasing short fiber content, indicating a higher degree of elasticity in the ductile phase for higher short fiber content prints when temperature exceeds the T_g. During the cooling cycle at the

commencement of the test, the recovered stress, while still increasing, was higher for the higher short fiber content prints. The culmination of these trials revealed that the MWCNT-based inks have the potential to generate high-strength prints, with strength increasing with increased short fiber content, all while retaining the demonstrated shape memory functionality.

There are numerous avenues through which this work can be expanded by focusing on the improvement of materials and manufacturing technologies. First, the electromechanical trials performed on MWCNT prints can be further investigated. Due to either the relatively low volume fraction of carbon, in the form of nanotubes and short fibers, or the poor distribution of those carbon components, the electromechanical response of the conductive MWCNT prints varied highly, often behaving sporadically. It would be worth pursuing the cause of that behavior and exploring if increased MWCNT content could help improve the viability of those prints as strain sensors [57, 58]. Since the electrical resistance of the developed nanocomposites can be tailored by adjusting the MWCNT concentrations, piezoresistive sensing functions can be developed and the sensors can be manufactured using 3D printing technologies [59]. Other critical material properties, such as thermal and mechanical properties, can be optimized by changing material formulation and altering the 3D printing parameters [60-62]. Moreover, for both MWCNT and carbon black inks, more work should be done to explore the effects of different material preparation and processing on the mechanical and electromechanical qualities of the prints. Since these inks are novel, a comparison between different combinations of sonication, shear mixing, and degassing should be investigated. Finally, thermogravimetric analysis (TGA) and differential scanning calorimetry (DSC) analysis

should be performed to complete the characterization of the novel MWCNT and carbon black inks.

Due to the unique properties and functionalities of the 3D printed shape memory composites, the developed materials can be further investigated for broad engineering applications. The piezoresistive sensing capability of the 3D printed materials can potentially be used as structural materials with real-time damage diagnostic and remaining useful life estimation functionalities, which are also commonly referred to as structural health monitoring and prognostics devices [63-68]. External load and environmental conditions applied to the 3D printed composites can be measured in real-time during service. All the recorded sensing data can be interpreted using data-driven and physics-based algorithms for the identification of damage in composites [69-74]. Certain real-time damage diagnostics and prognostics capabilities in structural composites can be extremely valuable by significantly increasing structural safety, reducing operational risk, extending structural service lives, and minimizing maintenance and repair costs.

Another potential application of the 3D printed shape memory composites is related to lightweight aerospace structures. Due to the flexibility of 3D printed geometries and the shape recovery properties, the developed technologies in this thesis can be potentially used for the design, development, and fabrication of lightweight aerospace grade composites with autonomous morphological optimization capabilities. Next-generation aerospace structures used in satellites and airplanes may require real-time optimization of structural geometries during service to improve energy efficiency, allow self-deployment, reduce signature, and obtain beneficial functionalities [75-77]. The reported methods in this thesis provide a new approach to manufacture certain novel engineering structures with minimal

costs and freedom to optimize material formulation based on the required product features. Novel materials development, characterization, modeling, manufacturing, and product design technologies can be matured based on the platform of material development and 3D printing approaches reported in this thesis [78-86].

References

1. W. Gao, Y. Zhang, D. Ramanujan, K. Ramani, Y. Chen, C.B. Williams, C.C.L. Wang, Y.C. Shin, S. Zhang, and P.D. Zavattieri, *The status, challenges, and future of additive manufacturing in engineering.* Computer-Aided Design, 2015. **69**: p. 65-89 %@ 0010-4485.
2. J. Zhang and Z. Yu, *Overview of 3D printing technologies for reverse engineering product design.* Automatic Control and Computer Sciences, 2016. **50**(2): p. 91-97 %@ 0146-4116.
3. T.D. Ngo, A. Kashani, G. Imbalzano, K.T.Q. Nguyen, and D. Hui, *Additive manufacturing (3D printing): A review of materials, methods, applications and challenges.* Composites Part B: Engineering, 2018. **143**: p. 172-196 %@ 1359-8368.
4. X. Wang, M. Jiang, Z. Zhou, J. Gou, and D. Hui, *3D printing of polymer matrix composites: A review and prospective.* Composites Part B: Engineering, 2017. **110**: p. 442-458.
5. T.D. Ngo, A. Kashani, G. Imbalzano, K.T. Nguyen, and D. Hui, *Additive manufacturing (3D printing): A review of materials, methods, applications and challenges.* Composites Part B: Engineering, 2018. **143**: p. 172-196.
6. M. Abshirini, M. Charara, P. Marashizadeh, M.C. Saha, M.C. Altan, and Y. Liu, *Functional nanocomposites for 3D printing of stretchable and wearable sensors.* Applied Nanoscience, 2019. **9**(8): p. 2071-2083.
7. A. Renteria, J.A. Diaz, B. He, I.A. Renteria-Marquez, L.A. Chavez, J.E. Regis, Y. Liu, D. Espalin, T.-L.B. Tseng, and Y. Lin, *Particle size influence on material properties of BaTiO3 ceramics fabricated using freeze-form extrusion 3D printing.* Materials Research Express, 2019. **6**(11): p. 115211.
8. A. Renteria, H. Fontes, J.A. Diaz, J.E. Regis, L.A. Chavez, T.-L.B. Tseng, Y. Liu, and Y. Lin, *Optimization of 3D printing parameters for BaTiO3 piezoelectric ceramics through design of experiments.* Materials Research Express, 2019. **6**(8): p. 085706.
9. J. Liu and C. Yan, *3D printing of scaffolds for tissue engineering*, in *3D Printing %@ 1789239664*. 2018, IntechOpen.
10. L.A. Chavez, B.R. Wilburn, P. Ibave, L.C. Delfin, S. Vargas, H. Diaz, C. Fulgentes, A. Renteria, J. Regis, and Y. Liu, *Fabrication and characterization of 3D printing induced orthotropic functional ceramics.* Smart Materials and Structures, 2019. **28**(12): p. 125007.
11. M. Charara, M. Abshirini, M.C. Saha, M.C. Altan, and Y. Liu, *Highly sensitive compression sensors using three-dimensional printed polydimethylsiloxane/carbon nanotube nanocomposites.* Journal of Intelligent Material Systems and Structures, 2019. **30**(8): p. 1216-1224.
12. L.A. Chavez, J.E. Regis, L.C. Delfin, C.A. Garcia Rosales, H. Kim, N. Love, Y. Liu, and Y. Lin, *Electrical and mechanical tuning of 3D printed photopolymer–MWCNT nanocomposites through in situ dispersion.* Journal of Applied Polymer Science, 2019. **136**(22): p. 47600.
13. W.M. Huang, Z. Ding, C.C. Wang, J. Wei, Y. Zhao, and H. Purnawali, *Shape memory materials.* Materials today, 2010. **13**(7-8): p. 54-61 %@ 1369-7021.

14. Y. Lu, W. Zhao, Z. Cui, H. Zhu, and C. Wu, *Journal of the Mechanical Behavior of Biomedical Materials.* Journal of the Mechanical Behavior of Biomedical Materials, 2018. **81**: p. 106-119.
15. J. Wang, R. Kunkel, J. Luo, Y. Li, H. Liu, B.N. Bohnstedt, Y. Liu, and C.-H. Lee, *Shape memory polyurethane with porous architectures for potential applications in intracranial aneurysm treatment.* Polymers, 2019. **11**(4): p. 631.
16. Z.G. Wei, R. Sandstroröm, and S. Miyazaki, *Shape-memory materials and hybrid composites for smart systems: Part I Shape-memory materials.* Journal of materials science, 1998. **33**(15): p. 3743-3762 %@ 0022-2461.
17. A. Lendlein and R. Langer, *Biodegradable, elastic shape-memory polymers for potential biomedical applications.* Science, 2002. **296**(5573): p. 1673-1676 %@ 0036-8075.
18. J. Wang, J. Luo, R. Kunkel, M. Saha, B.N. Bohnstedt, C.-H. Lee, and Y. Liu, *Development of shape memory polymer nanocomposite foam for treatment of intracranial aneurysms.* Materials Letters, 2019. **250**: p. 38-41.
19. J. Luo, R. Kunkel, J. Wang, B.N. Bohnstedt, M. Saha, Y. Liu, and C.-H. Lee. *Highly Porous Shape Memory Nanocomposites for Applications in Biomedical Devices*. in *ASME International Mechanical Engineering Congress and Exposition*. 2019. American Society of Mechanical Engineers.
20. J. Wang, J. Luo, R. Kunkel, Y. Liu, B. Bohnstedt, and C.-H. Lee. *Biomedical Devices Using Shape Memory Polymer Foams for Treatment of Intracranial Aneurysms*. in *ASME 2018 International Mechanical Engineering Congress and Exposition*. 2018. American Society of Mechanical Engineers Digital Collection.
21. J. Wang, S. Chowdhury, Y. Liu, B. Bohnstedt, and C.-H. Lee. *Development of thermally-activated shape memory polymers and nanocomposites for biomedical devices*. in *ASME 2017 International Mechanical Engineering Congress and Exposition*. 2017. American Society of Mechanical Engineers Digital Collection.
22. W. Sokolowski, S. Tan, P. Willis, and M. Pryor. *Shape memory self-deployable structures for solar sails*. 2008. International Society for Optics and Photonics.
23. J. Wang, D. Lee, and Y. Liu. *Joule-Heating Activated Flexible Composite Structures Using Shape Memory Epoxy*. in *ASME 2017 International Mechanical Engineering Congress and Exposition*. 2017. American Society of Mechanical Engineers Digital Collection.
24. Y. Liu, A. Rajadas, and A. Chattopadhyay. *Self-healing nanocomposite using shape memory polymer and carbon nanotubes*. in *Sensors and Smart Structures Technologies for Civil, Mechanical, and Aerospace Systems 2013*. 2013. International Society for Optics and Photonics.
25. H. Meng and G. Li, *A review of stimuli-responsive shape memory polymer composites.* Polymer, 2013. **54**(9): p. 2199-2221.
26. Q. Meng and J. Hu, *A review of shape memory polymer composites and blends.* Composites Part A: Applied Science and Manufacturing, 2009. **40**(11): p. 1661-1672.
27. Y. Liu, H. Lv, X. Lan, J. Leng, and S. Du, *Review of electro-active shape-memory polymer composite.* Composites Science and Technology, 2009. **69**(13): p. 2064-2068.

28. X. Wang, M. Jiang, Z. Zhou, J. Gou, and D. Hui, *3D printing of polymer matrix composites: A review and prospective.* Composites Part B: Engineering, 2017. **110**: p. 442-458 %@ 1359-8368.
29. M. Korger, J. Bergschneider, M. Lutz, B. Mahltig, K. Finsterbusch, and M. Rabe. *Possible applications of 3D printing technology on textile substrates*. 2016. IOP Publishing.
30. M.F. Afrose, S.H. Masood, P. Iovenitti, M. Nikzad, and I. Sbarski, *Effects of part build orientations on fatigue behaviour of FDM-processed PLA material.* Progress in Additive Manufacturing, 2016. **1**(1-2): p. 21-28 %@ 2363-9512.
31. Y. Yang, Y. Chen, Y. Wei, and Y. Li, *3D printing of shape memory polymer for functional part fabrication.* The International Journal of Advanced Manufacturing Technology, 2016. **84**(9): p. 2079-2095.
32. S. Olivera, H.B. Muralidhara, K. Venkatesh, K. Gopalakrishna, and C.S. Vivek, *Plating on acrylonitrile–butadiene–styrene (ABS) plastic: a review.* Journal of materials science, 2016. **51**(8): p. 3657-3674 %@ 0022-2461.
33. W. Liu, N. Wu, and K. Pochiraju, *Relationship Between Conductivities and Shape Memory Performance of FDM Composite Filaments.* 2017: p. V014T11A002.
34. R. Matsuzaki, M. Ueda, M. Namiki, T.-K. Jeong, H. Asahara, K. Horiguchi, T. Nakamura, A. Todoroki, and Y. Hirano, *Three-dimensional printing of continuous-fiber composites by in-nozzle impregnation.* Scientific reports, 2016. **6**: p. 23058 %@ 2045-2322.
35. W. Liu, N. Wu, and K. Pochiraju, *Shape recovery characteristics of SiC/C/PLA composite filaments and 3D printed parts.* Composites Part A: Applied Science and Manufacturing, 2018. **108**: p. 1-11 %@ 1359-835X.
36. K. Estelle, D. Blair, K. Evans, and B.A. Gozen, *Manufacturing of smart composites with hyperelastic property gradients and shape memory using fused deposition.* Journal of Manufacturing Processes, 2017. **28**: p. 500-507 %@ 1526-6125.
37. V. Slavković, N. Grujović, A. Dišić, and A. Radovanović. *Influence of Annealing and Printing Directions on Mechanical Properties of PLA Shape Memory Polymer Produced by Fused Deposition Modeling*. 2017.
38. T. Xie, X. Xiao, and Y.T. Cheng, *Revealing triple‐shape memory effect by polymer bilayers.* Macromolecular Rapid Communications, 2009. **30**(21): p. 1823-1827 %@ 1022-1336.
39. M. Bodaghi, A.R. Damanpack, and W.H. Liao, *Triple shape memory polymers by 4D printing.* Smart Materials and Structures, 2018. **27**(6): p. 065010 %@ 0964-1726.
40. W. Zhu, X. Ma, M. Gou, D. Mei, K. Zhang, and S. Chen, *3D printing of functional biomaterials for tissue engineering.* Current opinion in biotechnology, 2016. **40**: p. 103-112 %@ 0958-1669.
41. N. Bhattacharjee, A. Urrios, S. Kang, and A. Folch, *The upcoming 3D-printing revolution in microfluidics.* Lab on a Chip, 2016. **16**(10): p. 1720-1742.
42. think3D. *Digital Light Processing (DLP)*. Available from: https://www.think3d.in/digital-light-processing-dlp-3d-printing-service-india/.
43. A. Li, A. Challapalli, and G. Li, *4D Printing of Recyclable Lightweight Architectures Using High Recovery Stress Shape Memory Polymer*. Scientific Reports, 2019. **9**: p. 7621.

44. H. Wu, P. Chen, C. Yan, C. Cai, and Y. Shi, *Four-dimensional printing of a novel acrylate-based shape memory polymer using digital light processing.* Materials & Design, 2019. **171**: p. 107704 %@ 0264-1275.
45. Q. Mu, L. Wang, C.K. Dunn, X. Kuang, F. Duan, Z. Zhang, H.J. Qi, and T. Wang, *Digital light processing 3D printing of conductive complex structures.* Additive Manufacturing, 2017. **18**: p. 74-83 %@ 2214-8604.
46. M. Zarek, M. Layani, I. Cooperstein, E. Sachyani, D. Cohn, and S. Magdassi, *3D printing of shape memory polymers for flexible electronic devices.* Advanced Materials, 2016. **28**(22): p. 4449-4454 %@ 0935-9648.
47. M. Guvendiren, J. Molde, R.M.D. Soares, and J. Kohn, *Designing biomaterials for 3D printing.* ACS biomaterials science & engineering, 2016. **2**(10): p. 1679-1693 %@ 2373-9878.
48. M.P.a.M. Lab. *Fundamentals of Direct-Ink-Writing*. Available from: https://labs.wsu.edu/mpml/projects/.
49. K. Chen, X. Kuang, V. Li, G. Kang, and H.J. Qi, *Fabrication of tough epoxy with shape memory effects by UV-assisted direct-ink write printing.* Soft Matter, 2018. **14**(10): p. 1879-1886.
50. A.S. Wu, W. Small Iv, T.M. Bryson, E. Cheng, T.R. Metz, S.E. Schulze, E.B. Duoss, and T.S. Wilson, *3D Printed Silicones with Shape Memory.* Sci Rep, 2017. **7**(1): p. 4664.
51. G. Postiglione, G. Natale, G. Griffini, M. Levi, and S. Turri, *Conductive 3D microstructures by direct 3D printing of polymer/carbon nanotube nanocomposites via liquid deposition modeling.* Composites Part A: Applied Science and Manufacturing, 2015. **76**: p. 110-114 %@ 1359-835X.
52. J. Lewicki, J. Rodriguez, C. Zhu, M. Worsley, A. Wu, Y. Kanarska, J. Horn, E. Duoss, J. Ortega, W. Elmer, R. Hensleigh, R. Fellini, and M. King, *3D-Printing of Meso-structurally Ordered Carbon Fiber/Polymer Composites with Unprecedented Orthotropic Physical Properties.* Scientific Reports, 2017. **7**: p. 43401.
53. *Specimens*. 2016; Available from: https://www.datapointlabs.com/specimens/tensilebars.htm.
54. *SOLVAY THORNEL VMX-24*. Available from: https://www.900gpa.com/en/product/fiber/CF_0017A2523D?u=metric.
55. *Carbon nanotube, multi-walled*. Available from: https://www.sigmaaldrich.com/catalog/product/aldrich/901019?lang=en&region=US.
56. *Carbon, mesoporous*. Available from: https://www.sigmaaldrich.com/catalog/product/aldrich/699632?lang=en&region=US.
57. B. Herren, M. Charara, M.C. Saha, M.C. Altan, and Y. Liu, *Rapid Microwave Polymerization of Porous Nanocomposites with Piezoresistive Sensing Function.* Nanomaterials, 2020. **10**(2): p. 233.
58. W. Luo, M. Charara, M.C. Saha, and Y. Liu, *Fabrication and characterization of porous CNF/PDMS nanocomposites for sensing applications.* Applied Nanoscience, 2019. **9**(6): p. 1309-1317.

59. S.A. Chowdhury, M.C. Saha, S. Patterson, T. Robison, and Y. Liu, *Highly conductive polydimethylsiloxane/carbon nanofiber composites for flexible sensor applications.* Advanced Materials Technologies, 2019. **4**(1): p. 1800398.
60. S. Chowdhury, M. Olima, Y. Liu, M. Saha, J. Bergman, and T. Robison, *Poly dimethylsiloxane/carbon nanofiber nanocomposites: fabrication and characterization of electrical and thermal properties.* International Journal of Smart and Nano Materials, 2016. **7**(4): p. 236-247.
61. C. Feng, M. Zhang, and B. Bhandari, *Materials properties of printable edible inks and printing parameters optimization during 3D printing: A review.* Critical reviews in food science and nutrition, 2019. **59**(19): p. 3074-3081.
62. R. Udroiu and A. Nedelcu, *Optimization of additive manufacturing processes focused on 3D Printing.* Rapid Prototyping Technology—Principles and Functional Requirements; Hoque, ME, Ed, 2011: p. 1-28.
63. Y. Liu, S. Mohanty, and A. Chattopadhyay, *Condition based structural health monitoring and prognosis of composite structures under uniaxial and biaxial loading.* Journal of Nondestructive Evaluation, 2010. **29**(3): p. 181-188.
64. Y. Liu, S.B. Kim, A. Chattopadhyay, and D. Doyle, *Application of system-identification techniquest to health monitoring of on-orbit satellite boom structures.* Journal of Spacecraft and Rockets, 2011. **48**(4): p. 589-598.
65. J.P. Lynch and K.J. Loh, *A summary review of wireless sensors and sensor networks for structural health monitoring.* Shock and Vibration Digest, 2006. **38**(2): p. 91-130.
66. J. Ou and H. Li, *Structural health monitoring in mainland China: review and future trends.* Structural health monitoring, 2010. **9**(3): p. 219-231.
67. D. Montalvao, N.M.M. Maia, and A.M.R. Ribeiro, *A review of vibration-based structural health monitoring with special emphasis on composite materials.* Shock and vibration digest, 2006. **38**(4): p. 295-324.
68. Y. Liu and S. Nayak, *Structural health monitoring: State of the art and perspectives.* Jom, 2012. **64**(7): p. 789-792.
69. Y. Liu, M.Y. Fard, A. Chattopadhyay, and D. Doyle, *Damage assessment of CFRP composites using a time–frequency approach.* Journal of Intelligent Material Systems and Structures, 2012. **23**(4): p. 397-413.
70. Y. Liu and A. Chattopadhyay, *Low-velocity impact damage monitoring of a sandwich composite wing.* Journal of Intelligent Material Systems and Structures, 2013. **24**(17): p. 2074-2083.
71. J. Zou, Y. Liu, B. Shan, A. Chattopadhyay, and L.L. Dai, *Early damage detection in epoxy matrix using cyclobutane-based polymers.* Smart materials and structures, 2014. **23**(9): p. 095038.
72. C.R. Farrar and K. Worden, *Structural health monitoring: a machine learning perspective*. 2012: John Wiley & Sons.
73. C.R. Farrar and K. Worden, *An introduction to structural health monitoring.* Philosophical Transactions of the Royal Society A: Mathematical, Physical and Engineering Sciences, 2007. **365**(1851): p. 303-315.
74. K. Worden and G. Manson, *The application of machine learning to structural health monitoring.* Philosophical Transactions of the Royal Society A: Mathematical, Physical and Engineering Sciences, 2007. **365**(1851): p. 515-537.

75. Y. Liu, H. Du, L. Liu, and J. Leng, *Shape memory polymers and their composites in aerospace applications: a review.* Smart Materials and Structures, 2014. **23**(2): p. 023001.
76. B.T. Lester, T. Baxevanis, Y. Chemisky, and D.C. Lagoudas, *Review and perspectives: shape memory alloy composite systems.* Acta Mechanica, 2015. **226**(12): p. 3907-3960.
77. L. Santo, F. Quadrini, A. Accettura, and W. Villadei, *Shape memory composites for self-deployable structures in aerospace applications.* Procedia Eng, 2014. **88**: p. 42-47.
78. B. Koo, Y. Liu, J. Zou, A. Chattopadhyay, and L. Dai, *Study of glass transition temperature (Tg) of novel stress-sensitive composites using molecular dynamic simulation.* Modelling and Simulation in Materials Science and Engineering, 2014. **22**(6): p. 065018.
79. P. Marashizadeh, M. Abshirini, J. Wang, M.C. Saha, and Y. Liu, *Multiscale Modeling of fiber fragmentation process in Aligned Zno nanowires enhanced Single fiber composites.* Scientific Reports, 2019. **9**(1): p. 1-13.
80. P. Marashizadeh, M. Abshirini, M.C. Saha, and Y. Liu, *Multi-scale analysis of fiber-matrix interfacial enhancement in hybrid structural composites with aligned zinc oxide nanowires.* Materials Research Express, 2019. **6**(8): p. 0850c7.
81. M.Y. Fard, A. Chattopadhyay, and Y. Liu, *Nonlinear 3PB and 4PB flexural behavior and softening localization for epoxy resin E 863 using digital image correlation technique.* Experimental Techniques, 2016. **40**(1): p. 159-171.
82. M. Yekani Fard, A. Chattopadhyay, and Y. Liu, *Influence of load type and stress gradient on flexural strength of epoxy resin polymeric material.* Journal of aerospace engineering, 2014. **27**(1): p. 55-63.
83. M. Yekani Fard, Y. Liu, and A. Chattopadhyay, *Analytical solution for flexural response of epoxy resin materials.* Journal of Aerospace Engineering, 2012. **25**(3): p. 395-408.
84. H.A. Hegab, *Design for additive manufacturing of composite materials and potential alloys: a review.* Manufacturing Review, 2016. **3**: p. 11.
85. Ş. Yıldızhan, A. Çalık, M. Özcanlı, and H. Serin, *Bio-composite materials: a short review of recent trends, mechanical and chemical properties, and applications.* European Mechanical Science, 2018. **2**(3): p. 83-91.
86. D.-C. Pham, N. Sridhar, X. Qian, A.J. Sobey, M. Achintha, and A. Shenoi, *A review on design, manufacture and mechanics of composite risers.* Ocean Engineering, 2016. **112**: p. 82-96.